Journal of Quantitative Spectroscopy & Radiative Transfer 312 (2024) 108814

Contents lists available at ScienceDirect

Journal of Quantitative Spectroscopy and Radiative Transfer

journal homepage: www.elsevier.com/locate/jqsrt

The new σ-IASI code for all sky radiative transfer calculations in the spectral range 10 to 2760 cm^{-1}: σ-IASI/F2N

Guido Masiello [a,*], Carmine Serio [a], Tiziano Maestri [b], Michele Martinazzo [b], Fabrizio Masin [b], Giuliano Liuzzi [a], Sara Venafra [c]

[a] Scuola di Ingegneria, Università della Basilicata, Potenza, Italy
[b] Dipartimento di Fisica e Astronomia, Università di Bologna, Bologna, Italy
[c] Agenzia Spaziale Italiana, ASI, Roma, Italy

ARTICLE INFO

Keywords:
All sky fast code
Radiative transfer
Multiple scattering
Far infrared
IASI
FORUM

ABSTRACT

The paper describes a recently developed forward model (σ-IASI/F2N) to produce spectral radiances from the far to near-infrared spectrum (100 to 2760 cm^{-1}). The model is a pseudo-monochromatic radiative transfer tool that exploits lookup tables to compute the optical depths of atmospheric gas and clouds. Multiple scattering effects are accurately included in both the Far IR and Thermal IR by using a scaling method for cloud and aerosol radiative properties parameterized in terms of their effective radius, which allows them to be handled adopting the same formalism used in the clear sky. In this paper we apply a novel approach to a classical scaling method in the thermal IR relying on our improved parametrization of backscattering parameter over that used by Chou (Martinazzo et al., 2021), while in the Far IR a corrective term is introduced. The code is written in Fortran and runs on Unix-based (Linux and macOS) or MS Windows operating systems. σ-IASI/F2N can be used to develop custom versions of fast-forward modules for satellite instruments working in the infrared spectral range, such as the Far-Infrared Outgoing Radiation Understanding and Monitoring (FORUM) and the Polar Radiant Energy in the Far-InfraRed Experiment (PREFIRE) missions. We discuss the σ-IASI/F2N performance in simulating a set of ECMWF analyses at the global scale. For this purpose, we compare observations from the Infrared Atmospheric Sounding Interferometer (IASI) flying on MetOp B, and C. Results show that σ-IASI/F2N can easily ingest ECMWF analyses data and accurately reproduce cloud patterns. We also show that the difference between σ-IASI/F2N simulations and corresponding IASI observations is below 1 K in the 8–12 um window region, which is mainly affected by the water vapor continuum absorption and weak lines, while for night-time clear sky, the differences are below 0.3 K. again within the same window region.

1. Introduction

The σ-IASI radiative transfer method [1] is a monochromatic, fast code for calculating the Earth spectrum in the infrared and related Jacobian matrices. The code has been recently updated to extend the spectral range to the Far Infrared (FIR, down to 10 cm^{-1}) and to include new modules for calculations in the cloudy sky, which takes advantage of improvements (e.g., [2]) for the application of scaling methods (e.g., [3]) that parametrize the optical depth of ice and liquid water clouds and several aerosols species.

The extension to the FIR is motivated by the long-standing scientific interests in that spectral region (e.g., [4]), which the initiative of ESA and NASA have recently boosted by funding new missions such as the Far-Infrared Outgoing Radiation Understanding and Monitoring (FORUM, [5]), launching in 2027, and the Polar Radiant Energy in the Far-InfraRed Experiment (PREFIRE) mission [6], planned for launch in 2023. FORUM and PREFIRE will provide the first full spectral measurements of FIR radiation from orbit, filling a major gap in our knowledge of Earth's energy budget and the role of FIR radiation in Arctic warming, sea ice loss, ice sheet melting, and sea level rise.

The FORUM payload includes a Fourier Transform Spectrometer covering the spectral region 100 to 1600 cm^{-1} (6.25 to 100 μm), with an apodized spectral resolution of 0.5 cm^{-1} and expected sampling of 0.36 cm^{-1}. In contrast, PREFIRE has a Thermal IR Spectrometer (TIRS), covering the range 5–54 μm (185 to 2000 cm^{-1}) with a sampling of 0.84 μm, for a total of 64 channels.

* Corresponding author.
E-mail address: guido.masiello@unibas.it (G. Masiello).

https://doi.org/10.1016/j.jqsrt.2023.108814
Received 13 June 2023; Received in revised form 19 October 2023; Accepted 20 October 2023
Available online 23 October 2023

To bridge the gap with modern infrared hyperspectral instruments operating in nadir mode, such as AIRS (Atmospheric Infrared Sounder, e.g., Aumann et al., [7]), IASI (Infrared Atmospheric Sounder Interferometer, Hilton et al. [8]) IASI-NG (IASI Next Generation, Crevoisier et al. [9]), CrIS (Cross-track Infrared Spectrometer, Zavyalov et al. [10]) HIRAS (Hyperspectral Infrared Atmospheric Sounder (e.g., Serio et al. [11]), which cover the mid-to-near infrared (600 to 3000 cm^{-1}), we have developed a new version of σ-IASI radiative transfer model, which will be referred to as σ-IASI/F2N (where F2N stands for Far- to Near-infrared) in the rest of the paper.

The model σ-IASI/F2N covers the range of 100 to 2760 cm^{-1}. It is a monochromatic radiative transfer code that can be used with any infrared spectrometer/radiometer. The application to a given instrument mainly depends on its Instrument Spectral Response Function (ISRF). The radiance calculations in the cloudy sky rely upon an updated implementation of the simple analytical scaling method [3], which allows using the same formalism of gases transmittance calculations while still retaining the capability of considering multiple scattering. In addition, a Tang methodology [12] is adapted to simulate the radiance fields over the FIR spectral range by appropriate multiplicative coefficients to improve the radiance computations in the presence of multiple scattering.

Currently, the σ-IASI/F2N code can run in two modes: 1) the Chou or C-mode and 2) the Chou-Tang mode or C-T mode. The C-mode uses the Chou scaling approximation for the whole spectral range of 10 to 2760 cm^{-1}. It is known (e.g., [2]) that the Chou approximation tends to overestimate spectral radiances in the FIR, particularly below 600 cm^{-1}. For this reason, we have developed an appropriate correction to the Chou radiances originally suggested by Tang et al. [12], which works in the FIR.

In comparison to schemes that solve the scattering radiative transfer equation with suitable numerical methods, such as the doubling-adding and discrete ordinates methods [13,14], σ-IASI/F2N is faster while accurate enough for operational end-users (as it will be shown in this paper). In passing, we note that one of the most popular numerical schemes for multiple scattering, that is DISORT (Discrete Ordinate Radiative Transfer, Stamnes et al. [15]), has been coupled with LBLRTM (Line-by-Line Radiative Transfer Model, Clough et al. [16]) to yield LBLDIS [17]. We also note here the development of schemes specialized in retrieving the properties of cirrus clouds for a handful of spectral channels (e.g., [18]).

σ-IASI/F2N aims to take a step forward concerning those models that use approximate methodologies to treat scattering effects. Several works in the past few years (e.g., [19–23]). have discussed the applications and limitations of such models, and a recent comparison of radiative transfer codes for the cloudy sky has been provided by Aumann et al. [24].

The present study extends scaling methods for radiance calculation with scattering effects to the FIR. In addition, it describes a fully analytical scheme to compute analytical Jacobians for cloud parameters. The study is intended to support both FORUM and PREFIRE missions with a flexible radiative transfer code, which can be used for the science and operational analysis of observations. An assessment of the newly proposed Tang adjustment is provided at FIR wavelengths by comparing high spectral resolution radiances, in various atmospheric conditions, to the same quantities computed by using a physics scheme such as LBLDIS.

In addition to the FIR extension, we have also extensively evaluated the accuracy of the forward model calculations in C-mode, for the spectral range 645 to 2760 cm^{-1} using IASI observations on a global scale. The evaluation could not be extended to the C-T mode, given the lack of satellite observations in the FIR.

The IASI observations are collocated with ECMWF analysis fields, including the Temperature, humidity, ozone, and liquid and ice water content profiles. The ECMWF analysis profiles are used as inputs to σ-IASI/F2N to compute radiances, which are then compared to collocated IASI observations. The results show that the new σ-IASI/F2N can simulate cloudy radiances with a bias well below 1 K in brightness temperature along the whole IASI spectral range.

The paper is organized as follows. Section 2 deals with data and methods. Section 3 illustrates and describes the results of the C-mode evaluation in the mid-infrared. Finally, Section 4 is devoted to the conclusions.

2. Data and methods

IASI and ECMWF analysis fields have been used to define a global data set of pairs (Observations, Atmospheric State Vector). The ECMWF atmospheric state vector feeds the new σ-IASI/F2N, and the resulting radiances are used to compare with IASI observations. We stress that our exercise could have used many satellite infrared observations (including instruments such as AIRS and CrIS). However, we have limited to IASI because the full disk analysis could have become too computationally expensive and also because GSICS (Global Space-based Inter-Calibration System) has selected IASI-A/B/C for assessing infrared channels (e.g., Goldberg and Bali (2021), Serio (2021)).

2.1. The global ECMWF/IASI database

To have a validation dataset covering all latitudes/climate regions, we collocated measurements from MetOp-B and MetOp-C with ECMWF analyses. We use MetOp measurements from 23:45 on 8 September 2021 to 00:15 on 10 September 2021, which include MetOp-B orbits 46574-46589 and MetOp-C orbits 14732-14746. The selected measurements are associated with the ECMWF base time analyses. The temporal coincidence interval is set to +/- 15 min. With this criterion, we selected 16 MetOp orbits: 8 for MetOp-B (46574 46575, 46578, 46581,46582, 46585, 46588, 46589) and 8 for MetOp-C (14732, 14733, 14735, 14736, 14739, 14742, 14743, 14746).

The dataset consists of 270,200 IASI spectra, of which 167,244 are over the sea. These constitute the subset used for the intercomparison exercise to avoid biases arising from wrong assumptions about surface emissivity. We emphasize that this paper compares observations to simulations without retrievals, as we just compared measurements with simulations. The location of the IASI footprints over the sea is shown in Fig. 1. In addition, information about the acquisition time is provided in the color bar.

ECMWF analyses provide, for each IASI spectrum, surface temperature and Temperature profile (T), H_2O mixing ratio (Q), O_3 mixing ratio (O), Specific Liquid and Ice Water Content (q_w and q_i expressed in mass mixing ratio, kg/kg) over a pressure grid of 137 levels from the surface to 0.01 hPa. Fig. 1 shows the colocations of IASI observations within 15 min of ECMWF analysis model output. An overview of the meteorological conditions is shown in Fig. 2 where the integrated column of q_w and q_i at the global scale are plotted at the canonical noon.

The state vector ingested by the code is therefore the following:

$$v_{ECMWF} = (T, T_s, Q, O, D,\ q_w,\ q_i, tcc)$$

where, tcc is the total cloud cover, and D is the profile of HDO (heavy water), which is derived from Q by multiplying it by the abundance ratio D/Q prescribed by the Standard Vienna Mean Ocean Water (VSMOW) ratio, that is $R_{VSMOW} = 3.1 \times 10^{-4}$.

The state vector for σ-IASI/F2N requires additional parameters concerning the effective size of the liquid water and ice particles in cloud layers. The effective radius, r_e and dimension, D_e are obtained through the Martin formula [25] and the Wyser approach [26]. The definition of the thermodynamic, gas concentration values, and cloud properties in the model layer accounts for a different atmospheric layering between the code and the analyses. In fact, the ECMWF analyses is provided on 137 pressure levels, while σ-IASI/F2N works with a fixed pressure grid of 61 levels and 60 layers. More details are provided in Section 2.2.

Apart from the atmospheric parameter addressed above, for completeness, we recall that in the current version of σ-IASI/F2N, the

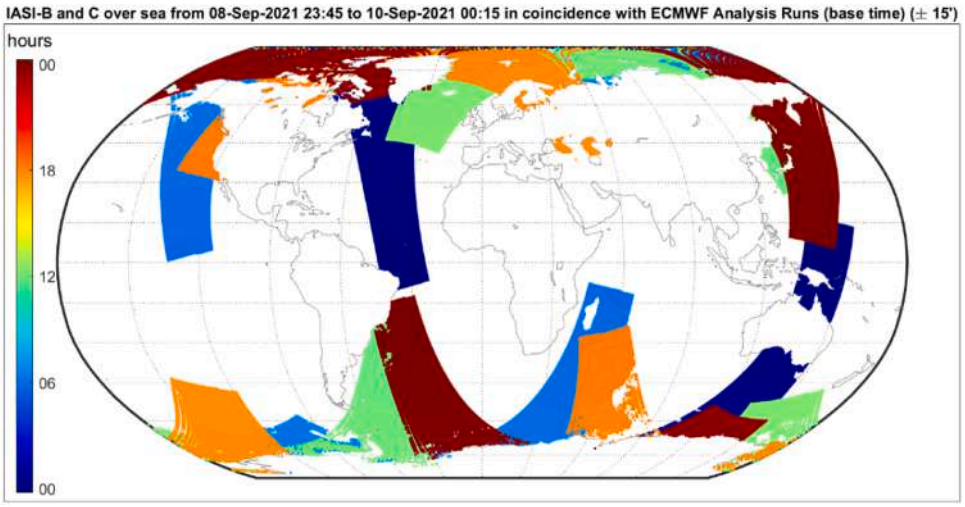

Fig. 1. IASI footprints in the database. The color indicates the IASI observations measurement time.

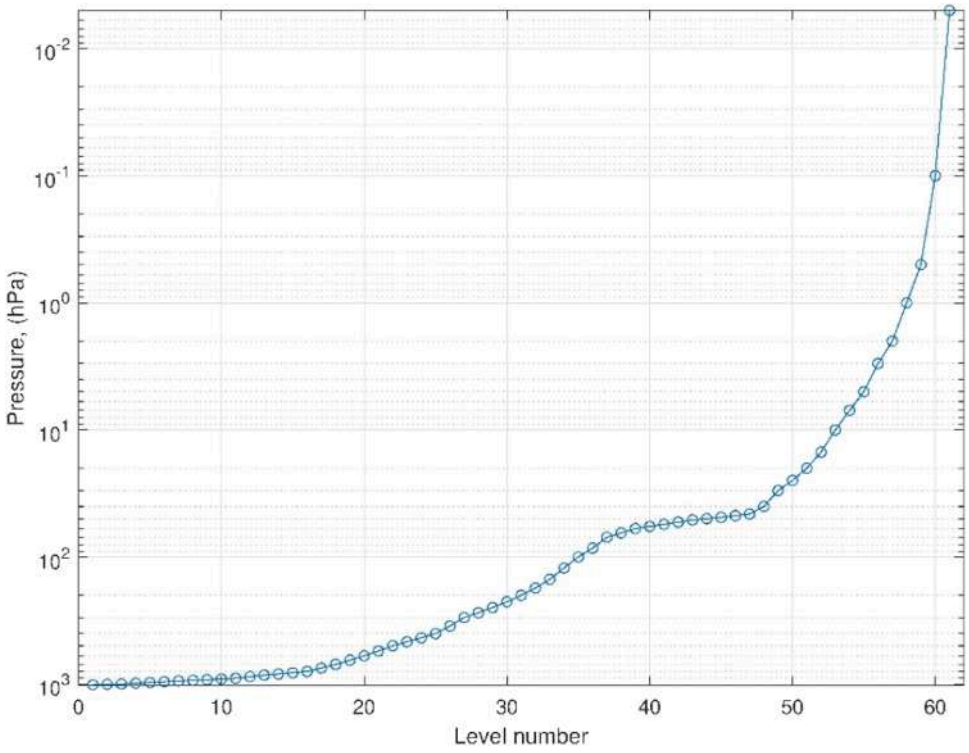

Fig. 2. The definition of the atmospheric pressure levels used in σ-IASI/F2N.

atmospheric state vector is specified by surface temperature (T_s) and emissivity spectrum, ε. For the atmosphere, we have atmospheric profiles of Temperature, $\boldsymbol{T}$ plus mixing ratio profiles, $\boldsymbol{q}$ of H_2O, HDO, O_3, CO_2, N_2O, CO, CH_4, SO_2, HNO_3, NH_3, OCS, and CF_4. The former profiles form the basis of state vector for clear sky, in the case of a cloudy sky, we have the additional profiles for the mass mixing ratio (or specific liquid and ice water content) q_w and q_i, respectively, and the related effective radius, r_e for *water cloud* and effective dimension, D_e for ice. The input state vector is summarized in Table 1

Table 1
List of the geophysical parameters included in the state vector of σ-IASI/F2N.

Vertical **profiles: size 60**				**Surface and scalars**
Temperature and gases			Clouds	
Temperature (K)	O_3 (ppv)	SO_2 (ppv)	q_w (kg/kg)	Emissivity Spectrum
H_2O (gr/kg)	N_2O (ppv)	HNO_3 (ppv)	q_i (kg/kg)	T_s (K)
HDO (ppv)	CO (ppv)	NH_3 (ppv)	r_e (μm)	tcc (scalar)
CO_2 (ppv)	CH_4 (ppv)	CF_4 (ppv)	D_e (μm)	

2.2. The basic radiative transfer in σ-IASI/F2N

The σ-IASI/F2N module is a *monochromatic, 1-D* radiative transfer model, which uses an appropriate atmospheric layering on which to

compute optical depths. The layering consists of a grid of vertical layers of constant pressure. The discretized version of the radiative transfer equation, solved within σ-IASI/F2N, uses a 60-layer pressure grid spanning the range 1100–0.005 hPa. The 61 atmospheric pressure levels, which divide the atmosphere into 60 layers, are shown in Fig. 3. Note the relatively higher density of layers at pressure levels just above the Tropopause. This is the optimal configuration to simulate data recorded by ground, orbit, or instruments on board an aircraft flying at about 20 km altitude [27]. The monochromatic optical depth calculation is based upon suitable lookup tables for atmospheric gases and clouds. For atmospheric gases, the lookup table is generated from LBLRTM v.12.7 [16], and related MT_CKD v. 3.2 for water vapor continuum absorption, whereas for clouds, we use LBLDIS [17].

Apart from parameters and species listed in Table 1 whose concentration can be varied and retrieved, σ-IASI/F2N also considers a set of fixed species that, although not retrieved, impact the simulated radiance in the forward model. This set includes the major species N_2 and O_2, which are considered through their collision-induced continuum (and very weak quadrupole or magnetic dipole lines). In addition, σ-IASI/F2N considers other trace gases, such as NO, NO_2, OH, HCl, H_2CO, HCN, CH_3Cl, and C_2H_2 (numbers 8, 10, 13, 15, 20, 23, 24, 26, respectively, in LBLRTM list of species). The vertical reference profiles of these molecules are fixed according to the U.S. Standard Atmosphere model [28]. Fixed gases also include heavy molecules whose radiative effect is modelled through cross-sections. The present work includes CCl_4, CFC-11, CFC-12, and HCFC-22. Their mixing ratio is assumed to be vertically uniform and scaled according to the 2015 report of WDCGG (World Data Centre for Greenhouse Gases) [29]. Finally, we use the water vapor

The σ-IASI/F2N forward model solves the radiative transfer equation in the form

$$R(\sigma) = R_s(\sigma) \ + R_a(\sigma) + R_r(\sigma) + R_i(\sigma) \tag{1}$$

where $R(\sigma)$ is the spectral radiance, decomposed in its surface term at the top of the atmosphere, $R_s(\sigma)$, atmospheric component, $R_a(\sigma)$, the downward infrared radiation reflected at the surface, $R_r(\sigma)$, and solar radiation reflected at the surface, $R_i(\sigma)$, respectively. All quantities depend on the wavenumber σ, and the dependence over the directional angle is implicit. In Eq. (1), the top-of-the-atmosphere surface term is

$$R_s(\sigma) = \varepsilon(\sigma) B(\sigma, T_s) \tau_o(\sigma) \tag{2}$$

with

τ_o: the total transmittance of the atmosphere (along a vertical path)
ε: the emissivity spectrum
T_s: the surface temperature
B: the blackbody Planck function

The atmospheric component is expressed as:

$$R_a(\sigma) = \int_0^{+\infty} B(\sigma, T) \frac{\partial \tau}{\partial z} dz \tag{3}$$

with z the vertical spatial coordinate and τ the transmittance from altitude z to $+\infty$.

The term $R_r(\sigma)$ is appropriately dealt with according to the surface type. For the sea surface, we use a specular model [30]:

$$R_r(\sigma) = (1-\varepsilon)\tau_o \int_{+\infty}^{0} B(\sigma, T) \frac{\partial \tau_*}{\partial z} dz = (1-\varepsilon)\tau_o^2 \int_0^{+\infty} B(\sigma, T) \frac{1}{\tau^2} \frac{\partial \tau}{\partial z} dz \tag{4}$$

where $\tau_*$is the transmittance from altitude z to $z = 0$, and we have $\tau\tau_* = \tau_o$. For land, we use a Lambertian (diffuse) model:

$$R_r(\sigma) = (1-\varepsilon)\tau_o \int_{+\infty}^{0} B(\sigma, T) \frac{\partial \tau_*^f}{\partial z} dz \tag{5}$$

with

$$\tau_*^f = 2 \int_0^1 \tau_*(\mu, z) \mu d\mu \tag{6}$$

where, as in Eq. (4), $\tau_*$is the transmittance from altitude z to $z = 0$ along the slant path in the direction$\mu = cos\theta$ (withθ the satellite zenith angle). The top-to-bottom transmittance τ_* should not be confused with the bottom-to-top transmittance τ. According to Elsasser [31] it is postulated that

$$\tau_*^f(\mu, z) = \tau_*(\overline{\mu}, z), \tag{7}$$

that is, the diffuse transmittance can be calculated as the transmittance function at a suitable cosine angle; the term $1/\overline{\mu}$ is referred to as the diffusivity factor. For practical calculations, the value $1/\overline{\mu} = 1.66$ (corresponding to an effective zenith angle of 52.96°) yields accurate results, which depend on the optical depth; the effective zenith angle is spectrally dependent. For optical depth below 1, exact and approximate (through Eq. (7)) calculations nearly coincide (e.g., [32]). However, for analyses, which need better accuracy, the spectral-dependent effective angle can be coded up in terms of rapidly evaluating exponential integrals of the third kind [33].

Using Eq. (7), for a Lambertian surface, the reflected term, $R_r(\sigma)$, is computed according to

$$R_r(\sigma) = (1-\varepsilon)\tau_o \int_{+\infty}^{0} B(\sigma, T) \frac{\partial \tau_*(\overline{\mu}, z)}{\partial z} dz \tag{8}$$

Finally, $R_i(\sigma)$, that is, the reflected sunlight at the surface is modeled through

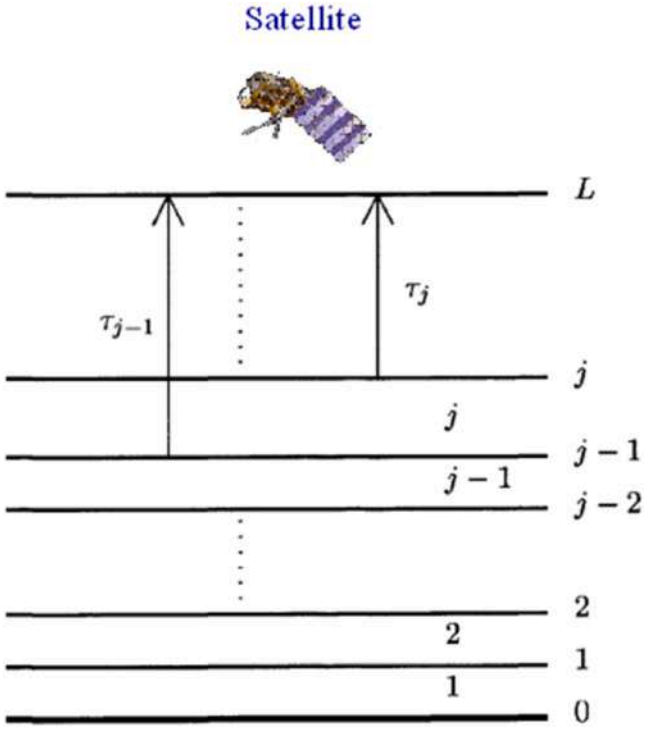

Fig. 3. The scheme shows the level and layering numbering convention used here.

$$R_i(\sigma) = r\left(\theta_{sun}, \theta_{sat}, v^2, \Phi\right)\tau_o^{sun}\tau_0^{sat}F_{sun} \tag{9}$$

in case of a water body, in which case $r(\theta_{sun},\theta_{sat},v^2,\Phi)$ is the bidirectional reflectance distribution function according to the Cox-Munk model [34]; in this case, θ_{sat} and θ_{sun} are the satellite and Sun zenith angles respectively, v^2 is a wind speed parameter, and $\Phi = \phi_{sat} - \phi_{sun}$ is the difference of sun and satellite azimuth angles; moreover, F_{sun} is the monochromatic stellar (solar) irradiance.

In the case of a Lambertian diffuser, Eq. (9) becomes

$$R_r(\sigma) = r\tau_o^{sun}\frac{F_{sun}\mu_{sun}}{\pi}\tau_0^{sat} = \left(1-\varepsilon_g\right)\tau_0^{sat}\tau_o^{sun}\frac{F_{sun}\mu_{sun}}{\pi} \tag{10}$$

We also note that $\tau_0^{sat}\tau_o^{sun} = \left(\tau_0^{sat}\right)^{\left(1+\frac{\mu_{sat}}{\mu_{sun}}\right)}$.

For numerical calculation, we need to compute the *atmospheric emission* integral of Eq. (3) and its downwelling counterpart appearing in Eq. (4) and Eq. (8). To this end, considering the atmospheric layering shown in Fig. 3 and adopting the approximation of parallel-plane atmosphere (Fig. 4), the upwelling thermal radiation of Eq. (3) can be approximated according to

$$R_a(\sigma) \approx \sum_{j=1}^{L}\left(\int_{z_{j-1}}^{z_j} B(T)\frac{\partial\tau}{\partial z}dz\right) \tag{11}$$

and using the *mean value theorem,* e.g., (Smirnov, n.d.) we can analytically compute the integral,

$$\int_{z_{j-1}}^{z_j} B(T)\frac{\partial\tau}{\partial z}dz = B(T(z^*))\left(\tau_j - \tau_{j-1}\right), \quad \text{with } z_{j-1} \le z^* \le z_j \tag{12}$$

We note that z^* can depend on the wavenumber. A formal derivation of Eq. (12) and the way we deal with the term $B(T(z^*))$ are shown in the appendix. A similar treatment is performed with the downwelling thermal radiation integral.

For a clear sky, the σ-IASI/F2N forward model strictly applies to the case of a non-scattering atmosphere, which is a good approximation for a clear sky, where only the absorption by atmospheric gas is considered. In presence of clouds and aerosols, a *source* function is needed to properly deal with multiple scattering [32]. Our approach is to use the scaling approximation introduced by Chou et al. [3], which allows to consider multiple scattering while still using the radiative transfer equations for a clear atmosphere. In this way, the difficulties in applying a multiple-scattering algorithm to a partly cloudy scene are avoided, and the computational efficiency is comparable to that for a clear scene. The details on the approach used in cloudy sky are provided in the next section.

2.2.1. Transmittance calculations and the optical depth lookup table

Transmittances in clear-sky and cloudy cases are defined according to the considered absorbers. In σ-IASI/F2N, it is assumed that the clear-sky transmittance is affected both by gas and aerosol particles, namely assuming that aerosols are uniformly distributed on the entire Field of View or FOV. The cloudy portion of the FOV will be additionally affected by the extinction due to water and ice clouds. To combine them, we assume the additive model

$$R(\sigma) = (1-f)R_{clear-sky} + fR_{cloudy-sky} \tag{13}$$

being f the cloud fraction, so that $f = 0$ means a clear FOV and $f = 1$ is a fully overcast FOV. Eq. (13) implements the maximum overlap model and says that the cloudy spectra are calculated as the linear combination of clear and cloudy columns based on the cloud fraction. $R(\sigma)$ is the spectrum calculated with the maximum overlap assumption and f is defined as the maximum cloud fraction in the cloud coverage profile. We set f equal to the total cloud cover (tcc) specified in the ECMWF record. $R_{clear-sky}$ is the clear-sky spectrum, and $R_{cloudy-sky}$ is the spectrum assuming full overcast (i.e., clouds fill the entire satellite footprint).

The general expression for the transmittance at pressure level j can be expressed as

$$\tau_j = \prod_{i=j+1}^{N} e^{-\left(\nu_{gas,i}+\nu_{aerosol,i}+\nu_{cloud,i}\right)} \tag{14}$$

where ν is the layer optical depth of the given parameter or species.

For atmospheric gas and aerosols, we refer to the papers by Amato et al. [1] and by Liuzzi et al. [20].

Here we remark that the gas optical depth for the atmospheric gases is computed based on a monochromatic Lookup Table (LUT) generated by the forward model LBLRTM version 12.7 and the line database AER v.

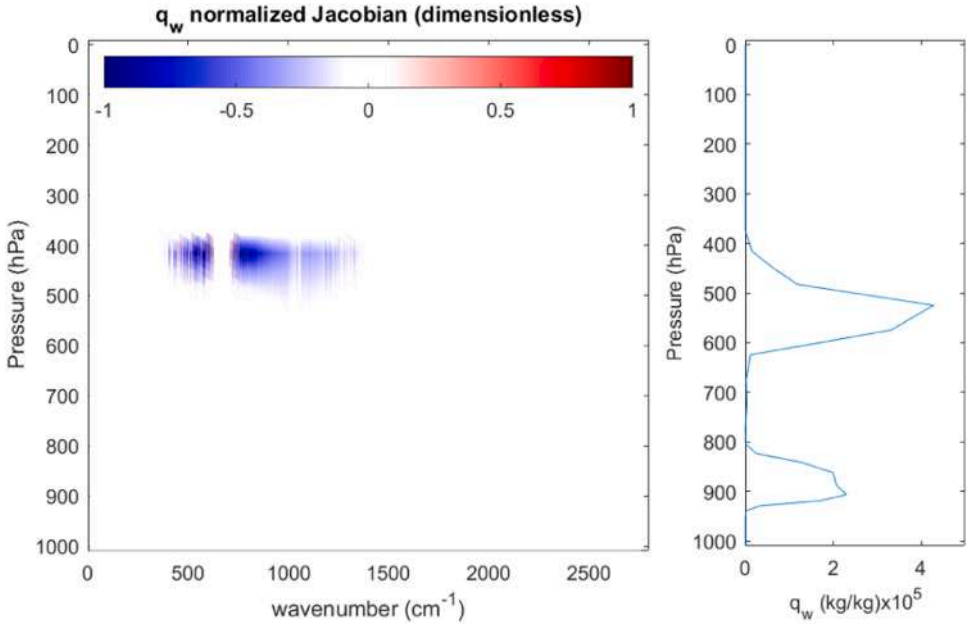

Fig. 4. Example of Jacobian (left) for the parameter q_w, whose profile is shown in the right panel.

3.2 (e.g., see the website http://rtweb.aer.com/main.html). The LUT based on LBLRTM covers the spectral range of 5 to 2760 cm^{-1}, and the sampling is $\Delta\sigma = 0.01$ cm^{-1}. This sampling is optimized for nadir-sounding sensors such as IASI and FORUM, primarily sensitive to the lower atmosphere and Troposphere, where pressure broadening widens the absorption line widths of molecular species. We also have a LUT with $\Delta\sigma = 0.001$ cm^{-1}, which is used for trade-off analysis between spectral resolution and accuracy when we add new spectral segments. It is important to note that even with the coarser sampling rate, since the LUT database was built starting from the resolution of $2\ 10^{-4}$ cm^{-1} [35], the code shows a greater sensitivity to the stratosphere to other non-monochromatic fast models [36]. This analysis is ongoing for the far-infrared portion of the spectrum.

For aerosol, using the same formalism that we are going to show in the next section, we have generated a LUT for dust like and volcanic dust, which can have a range of radii between 0.15–3μm. Again details are given in [2]. The aerosol is considered for analysis of heavy Saharian desert storms, which can transport dust like aerosol over the Mediterranean basin or volcanic eruptions. These situations are not the present study's focus, and the aerosol profile has been set to zero for all calculations considered in the present analysis.

The next section focuses on the formulation and parameterization of the optical depth for water and ice clouds, which is new and innovative concerning previous references.

2.2.2. Cloud optical depth parameterization, the C-mode

This section will discuss how the optical depth for clouds is parameterized within the forward module σ-IASI/F2N. We first deal with the Chou scaling approximation [3] then we will show how the former approximation is Tang-corrected [12].

The considered cloud layers include liquid water and ice clouds. The single scattering optical properties are selected using state-of-art databases or produced in-house using referenced codes. In the case of liquid water clouds, water spheres are assumed to be the primary constituent, and the macrophysical spectral quantities are generated through the Scattnlay model (Peña and Pal, 2009). The model utilizes complex refractive indexes (Downing and Williams, 1975) to solve the Mie scattering problem and obtain the desired properties. The code also allows to compute mixed phase particles constituted by an ice core with a liquid water coating. Results concerning mixed phase are not presented in this paper, since we are limited by the state vector as provided by ECMWF analyses.

Ice clouds are assumed to be composed by ice crystals, specifically column aggregates of hexagonal columns. The reference database is the Yang database (Yang et al., 2013) which accounts for 8 different pristine habits.

The considered single-particle single-scattering optical properties are then combined according with realistic particle size distributions (PSDs). Multiple lognormal size distributions (Miles et al., 2000) are used for liquid water clouds while, as commonly used, a set of modified gamma distributions are assumed in case of ice clouds.

Below is a description of the bulk (macrophysical) quantities. The effective size, D_e, of the PSD is defined according to [14]

$$D_e = \frac{3}{2}\frac{\int_{L_{min}}^{L_{max}} V(L)n(L)dL}{\int_{L_{min}}^{L_{max}} A(L)n(L)dL} \tag{15}$$

where

L: is the largest size of the particle

$n(L)$: is the probability density distribution of the particles

$V(L)$: is the volume of a particle of size L

$A(L)$: is the projected area of the particle with size L

For spherical particles, Eq. (15) becomes similar to the definition given by [37], that is $D_e = 2r_e$, which is the effective diameter of the particle.

According to the classical treatment for the definition of the cloud optical depth (e.g., [32]; Yang et al., 2001), we define the extinction coefficient χ which, net of the geometrical path Δz, yields the optical depth, OD:

$$\frac{OD}{\Delta z} = \chi = \int_{L_{min}}^{L_{max}} Q_e(L)A(L)n(L)dL \tag{16}$$

with

Q_e: the Mie single scattering extinction (scattering+absorption) efficiency,

Next, let us define the liquid water (ice) content at a given pressure level according to

$$xwc = \rho_x \int_{L_{min}}^{L_{max}} V(L)n(L)dL \tag{17}$$

where the ρ_x is the density of water, and x stands indifferently for *ice* or *liquid water*. Using both Eqs. (16) and (17), after a bit of algebra we arrive at the basic formula for the optical depth,

$$\frac{\frac{OD}{\Delta z}}{(xwc/\rho_x)} = \frac{\frac{\int_{L_{min}}^{L_{max}} Q_e(L)A(L)n(L)dL}{\int_{L_{min}}^{L_{max}} A(L)n(L)dL}}{\frac{2}{3}D_e} = \frac{3}{2}\frac{\beta}{D_e} \tag{18}$$

With the PSD extinction efficiency β defined as:

$$\beta = \langle Q_e \rangle = \frac{\int_{L_{min}}^{L_{max}} Q_e(L)A(L)n(L)dL}{\int_{L_{min}}^{L_{max}} A(L)n(L)dL} \tag{19}$$

which is the basic form we use in σ-IASI/F2N for calculating the optical depth of ice/water clouds. Eq. (19) strictly applies to single scattering. The inclusion of multiple scattering effects is obtained by considering the Chou scaling approximation [3], which demands that the extinction β is changed to $\widetilde{\beta}$, according to

$$\widetilde{\beta} = \beta((1-\omega) + \omega b) \tag{20}$$

with

$$\omega = \frac{\int_{L_{min}}^{L_{max}} (Q_e(L) - Q_a(L))A(L)n(L)dL}{\int_{L_{min}}^{L_{max}} Q_e(L)A(L)n(L)dL} \tag{21}$$

and b, the so-called Chou back-scattering parameter, is computed according to the appropriate phase function, P,

$$b = \frac{1}{2}\int_0^1 d\mu \int_{-1}^0 P(\mu, \mu', D_e)d\mu' \tag{22}$$

Martinazzo et al. [2] have shown that a correct calculation and parameterization of the back-scattering coefficient, b is crucial when applying the Chou scaling method to compute spectral radiances. In effect, the original formulation by [3] is intended for flux calculations, while applying to spectral radiances deserves more care in choosing and defining the appropriate phase function, P and the optical properties of liquid and ice particles.

Finally, we have

$$\frac{OD}{\Delta z} = \chi = \frac{3}{2}\frac{xwc}{D_e\rho_x}\widetilde{\beta} \tag{23}$$

In Eq. (23) xwc is the so-called Liquid water content LWC (or IWC in case of ice clouds), expressed in units of kg/m^3. LWC and IWC are easily derived from the specific liquid and ice contents values normally available from Numerical Weather Prediction centers (e.g., ECMWF) which are given as the mass mixing ratio (kg/kg)

$$q_x = \frac{m_x(mass\ of\ x)}{m_a(mass\ of\ air)} \tag{24}$$

This can be transformed in the units of kg/m^3 according to

$$xwc = q_x\rho_a,\ \rho_a = \frac{p}{R_aT} \tag{25}$$

where p, T, are the pressure and Temperature of air and R_a, is the gas constant for dry air, equal to 287.05 J kg^{-1}K^{-1}. To simplify notation, we put $r_e = D_e/2$ and Eq. (23) becomes

$$\frac{OD}{\Delta z} = \chi = \frac{3}{4}\frac{xwc}{r_e\rho_x}\tilde{\beta};\ (\text{units}:\ \text{m}^{-1}) \tag{26}$$

The apparent extinction coefficient (layer normalized optical depth) of Eq. (26) can be computed once we have β, b, ω, which depend on both the wavenumber and the effective radius, r_e.

The parameters β, b, ω have been pre-computed according to the methodology implemented by Martinazzo et al. [2]. All the parameters have been parameterized with 6th degree polynomials of the effective radius:

$$Y = \sum_{i=1}^{7} P_i x^{i-1};\ x = \frac{1}{r_e + t} \tag{27}$$

with P_i,t, depending on the wavenumber and where Y stands for β, b, ω. As a result, all the parameters that define the cloud properties in the layer (β, b, ω) are functions of the wavenumber and effective radius. This way we produce a LUT that contains the coefficients P_i,and$t$ as a function of the wavenumber from which the essential optical properties are derived.

The polynomial interpolation of the LUT facilitates the calculation of the derivatives of the optical depth for both mass content, q_x, and effective radius, r_e.

We have that:

$$\frac{\partial\chi}{\partial q_x} = \frac{3}{4}\frac{\rho_a}{r_e\rho_x}\tilde{\beta} = \frac{\chi}{q_x};\ \text{unitsof m}^{-1}\,(kg/kg)^{-1} \tag{28}$$

$$\frac{\partial\chi}{\partial r_e} = -\frac{3}{4}\frac{xwc}{r_e^2\rho_x}\tilde{\beta} + \frac{3}{4}\frac{xwc}{r_e\rho_x}\frac{\partial\tilde{\beta}}{\partial r_e}\ \text{unitsof m}^{-1}\,\mu\text{m}^{-1} \tag{29}$$

$$\frac{\partial\tilde{\beta}}{\partial r_e} = \frac{\partial\beta}{\partial r_e}[(1-\omega) + b\omega] + \beta\left[\frac{\partial\omega}{\partial r_e}(b-1)\right] + \beta\omega\frac{\partial b}{\partial r_e} \tag{30}$$

The derivatives $\frac{\partial\beta}{\partial r_e}, \frac{\partial\omega}{\partial r_e}, \frac{\partial b}{\partial r_e}$ can be easily obtained based on the polynomial parameterization:

$$\frac{\partial Y}{\partial r_e} = \frac{\partial Y}{\partial x}\frac{\partial x}{\partial r_e} = -\frac{1}{x^2}\sum_{i=1}^{7}(i-1)P_i x^{i-2} \tag{31}$$

where, as before, Y stands for β, b, ω. Note that the derivative with respect to the ice/liquid content (Eq. 28) is just the scaling of the extinction coefficient to the given concentration.

Eq. (26) is the basic expression of the extinction coefficient used to calculate transmittances, which are needed for the radiance calculations. Eqs (28) and (31) are required for further implementation in the code to compute spectral radiance derivatives for q_w,q_i,r_e,D_e. Because clouds are dealt with the same way as gases, the math to compute radiance derivatives is the same as that for gases (as in [1]).

Figs. 4-7 show an example of the Jacobian matrices over the full range of 10 to 2760 cm^{-1} for the cloud parameters. The Jacobian matrices correspond to a tropical atmosphere and the details of the profiles for q_w,q_i,r_e,D_e are provided in the figures as well. The cloud structure is rather complex. The example deals with a double-layer water cloud, with the upper layer centered at ~500 hPa showing a water/ice mix phase, and an uppermost cirrus cloud at ~200 hPa. Figs. 4-7 demonstrate that σ-IASI/F2N is capable of ingesting the full q_w, q_i,r_e,D_e state vector from the ECMWF model fields.

In Figs. 4-7, the Jacobian derivatives are normalized to their absolute maximum value. The normalization yields functions ranging between [−1,1]. The choice simplifies the graphic rendering and allows us to understand which spectral range is larger sensitive to the given parameter. For example, in tropical atmosphere where the water vapor concentration is high, all the cloud parameters show the highest sensitivity in the atmospheric window between 8 and 12 μm, and in the water vapor rotation band at around 20 μm. It should be noted that the vibration water vapor band at 6.7 μm is completely saturated and does not show any important sensitivity to cloud properties, demonstrating the importance of the FIR for cloud studies.

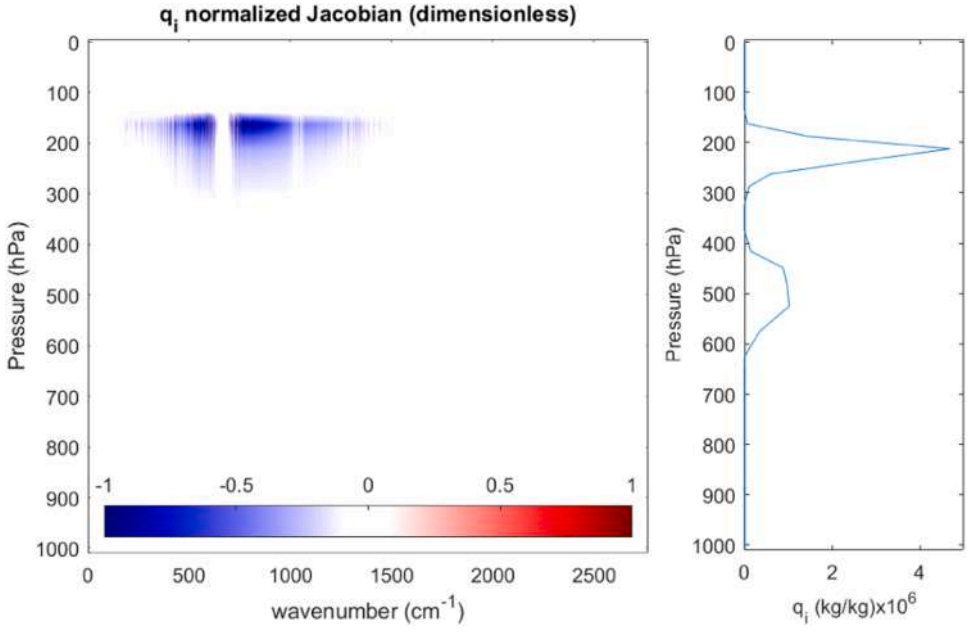

Fig. 5. Example of Jacobian (left) for the parameter q_i, whose profile is shown in the right panel.

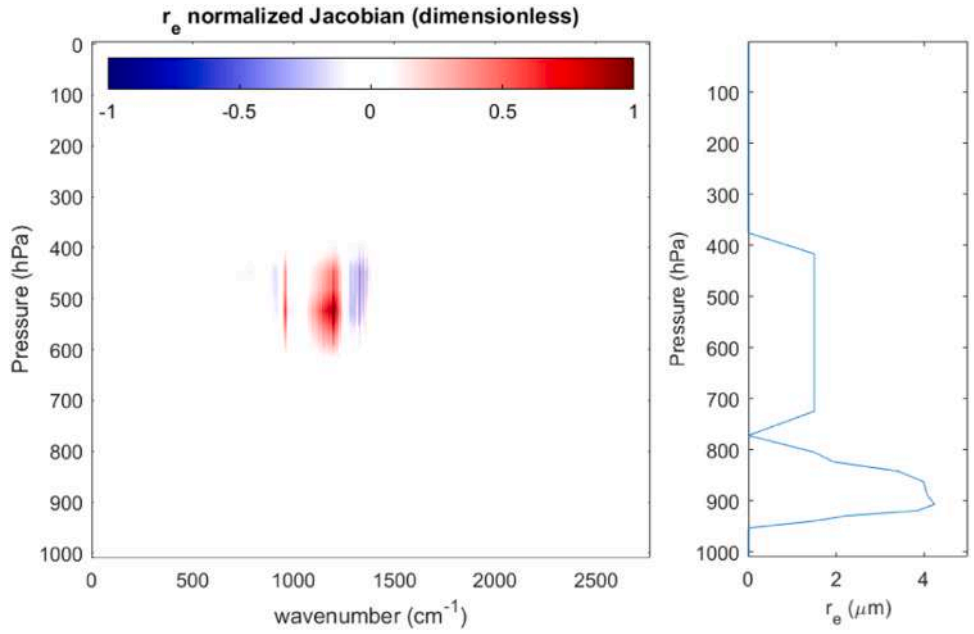

Fig. 6. Example of Jacobian (left) for the parameter r_e, whose profile is shown in the right panel.

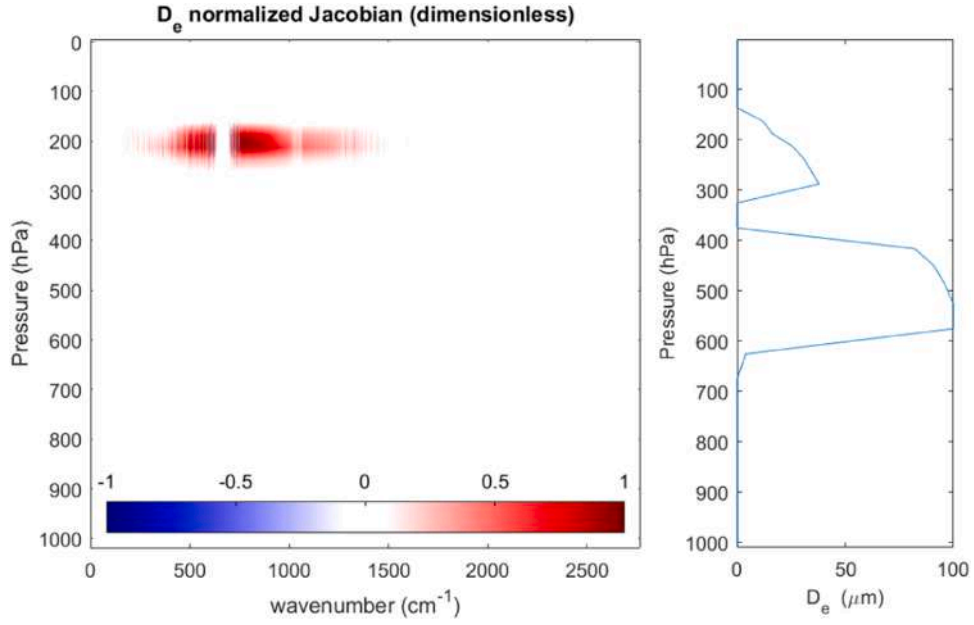

Fig. 7. Example of Jacobian (left) for the parameter D_e, whose profile is shown in the right panel.

2.2.3. The C-T mode

As mentioned in the previous sections, in σ-IASI/F2N the radiance calculation in cloudy sky conditions depend on an implementation of a simple analytical scaling method [3]. This methodology, originally developed in the context of broadband fluxes computation, has been proven to be suitable for the simulation of the upwelling radiances over the entire mid-infrared region [2]. Nevertheless, the extension of this solution to the FIR results in an overestimation of the upwelling radiances, especially in presence of ice (thus, also cirrus) clouds. In the perspective of the coming applications to FORUM and PREFIRE, we have also developed a correction scheme to the Chou method, which has been implemented as an additional routine to improve the flexibility of σ-IASI/F2N.

The correction term is modelled starting from the adjusted scheme proposed by Tang [12], to mitigate the computational errors of this basic scaling method in the FIR for any observational angles. In addition, an analysis is carried out to assess the effectiveness of this correction term to improve the spectral radiance simulations.

In the paper by Tang et al. [12] the cause of the radiance overestimation in the Chou method is recognized to lie in the main approximations made when the scaling method is introduced. The Chou approximation assumes that the downward ambient radiation, which scatters back from the layer in the upward direction, is equivalent to the Planckian emission originating from the layer itself. This assumption can lead to a large bias, as the actual downward ambient radiation is much weaker than the layer blackbody radiance. Tang's proposed adjustment scheme incorporates a correction term that reflects a more realistic depiction of the downward ambient radiation. The equations governing

the radiative transfer are modified as follows:

$$\begin{cases} \mu \dfrac{dR(\mu,z)}{dz} = -I + B, & \mu < 0 \\ \mu \dfrac{dR(\mu,z)}{dz} = -I + B + \dfrac{\omega b}{1-\omega(1-b)}[R(-\mu,z) - B], & \mu > 0 \end{cases} \tag{32}$$

First, the downward radiance ($\mu < 0$) is calculated using the Chou scheme. Successively, the upward radiance ($\mu > 0$) is computed also using the knowledge of the downward radiation $R(-\mu, z)$. Exploiting the properties of linear differential equations, a correction term for the upward radiance contribution of a uniform layer j can be obtained from Eq. (35) as:

$$R_j^c = \frac{1}{2}\frac{\omega b}{1-\omega(1-b)}\left[\left(R_j(-\mu) - B_j\right) - \left(R_j(-\mu) - B_j\right)\tau_j^2\right] \tag{33}$$

where $R_j(-\mu)$ is the downward radiance at the top of the considered layer, and τ_j is the layer transmissivity.

To extend the applicability of this method to radiance computations, a correction coefficient $k(\mu)$ is computed through numerical simulations (see below). This coefficient is then employed to replace the existing 1/2 coefficient in Eq. (33), resulting in improved accuracy of the radiance calculations.

$$R_j^{ck} = k(\mu)\frac{\omega b}{1-\omega(1-b)}\left[\left(R_j(-\mu) - B_j\right) - \left(R_j(-\mu) - B_j\right)\tau_j^2\right] \tag{34}$$

Where the superscript ck indicates the use of the coefficient in this correction term. The total correction for the radiation at the top of the atmosphere is obtained by summing all the correction terms attenuated by the layers of atmosphere between them and the satellite:

$$R^{ck} = \sum_{j=1}^{N} R_j^{ck} \cdot \tau \tag{35}$$

A similar equation holds for the R^c.

The coefficient $k(\mu)$ depends on the observational angle (i.e., FOV). A set of $k(\mu)$ is produced starting from accurate simulations obtained with the DISORT model [15]. We consider three climatological atmospheric profiles taken from the Level 2 Initial Guess (IG2) database (high- mid- and low-latitude). We perform nadir-looking simulations for each profile considering different cloud altitudes, optical depths, and effective radii. Then, for each case, we compute the residuals. ΔR_{chou} between the DISORT solution R_{DISORT} obtained using a number of streams equal to 18 and Chou's solution R_{chou}.

$$\Delta R_{chou}(\mu) = R_{DISORT}(\mu) - R_{chou}(\mu) \tag{36}$$

Along with this, we calculate the correction term R^c for the same scenario. The coefficients $k(\mu)$ are then obtained as the ratio between the Chou residuals and the original correction term, integrated over the FIR spectral interval between σ_1=100 cm^{-1} and σ_2=667 cm^{-1}:

$$k(\mu) = \frac{1}{2}\frac{\int_{\sigma_1}^{\sigma_2} \Delta R_{chou}(\mu) d\sigma}{\int_{\sigma_1}^{\sigma_2} R^c(\mu) d\sigma} \tag{37}$$

As with the other optical properties used by σ-IASI/F2N, the coefficients are parametrized as a function of the effective radius of the particle size distribution. Specifically, they are interpolated with the following function:

$$k(r_{eff}, \mu) = P_0(\mu) + P_1(\mu)\frac{1}{r_{eff}} + P_2(\mu)\frac{1}{r_{eff}^2} \tag{38}$$

Fig. 8 shows the values of these coefficients for all the simulations (green dots) performed considering a viewing angle $\mu = 1$. The interpolated function (Eq. 38) is shown as a solid black line in the same panels.

The effectiveness of the newly parameterized coefficient k for Tang's adjustment routine is tested over a wide set of simulations, considering different profiles from those used for the definition of k. Fig. 9 highlights the discrepancies ΔR between the full-physics solution R_a and the two approximate methodologies considered R_f: Chou's approximation (upper panels) and Tang's adjustment scheme with the k coefficients introduced. The discrepancies are computed as:

$$\Delta R = R_a - R_f \tag{39}$$

considering a mid-latitude atmosphere with a single-layer ice cloud.

In the same figure, the green dashed-dotted line represents the parameterization of the effective radius of the ice cloud as a function of temperature and total ice water content. This parameterization is based on Sun and Rikus' (1999) work, which was subsequently revised by Sun (2001). Similar results are obtained considering different atmospheric profiles (not shown for brevity).

Applying the new methodology improved the radiance residuals across a wide range of naturally occurring cloudy cases. Specifically, using the Tang methodology with the updated coefficients proves to be highly accurate in computing radiance fields in the presence of thin cirrus clouds, a key focus of the FORUM mission. In addition, it is important to note that the multiplicative coefficients are calculated not only for the zenith viewing angle but also for four additional Gaussian angles (not displayed), allowing for a comprehensive angular

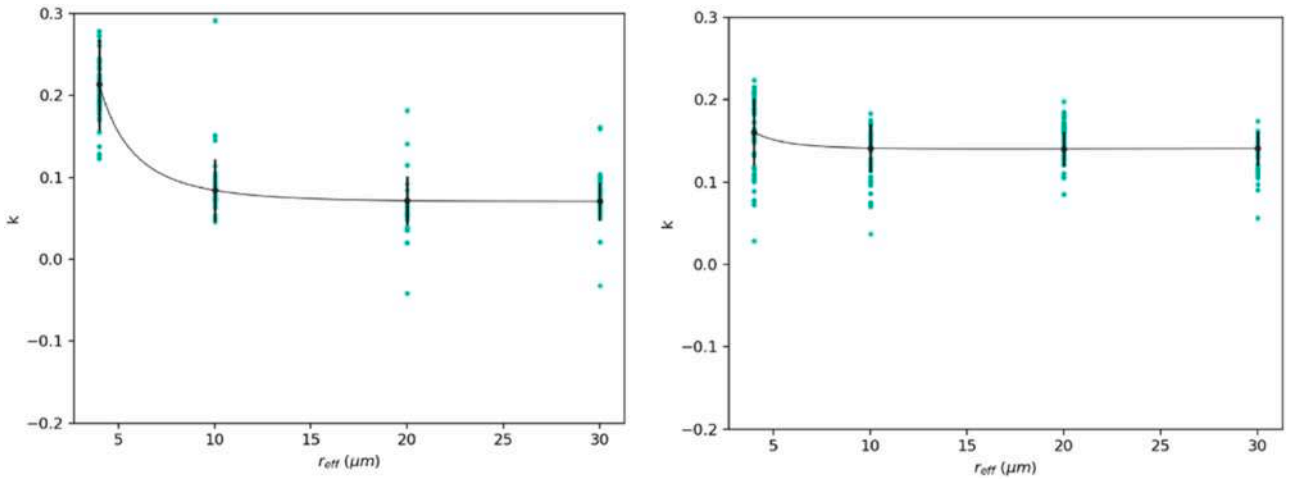

Fig. 8. Coefficients for water spheres (left panel) and column aggregates (right panel)as a function of the effective radius[μm]. The black solid line represents the parameterization as a function of the effective radius of the PSD.

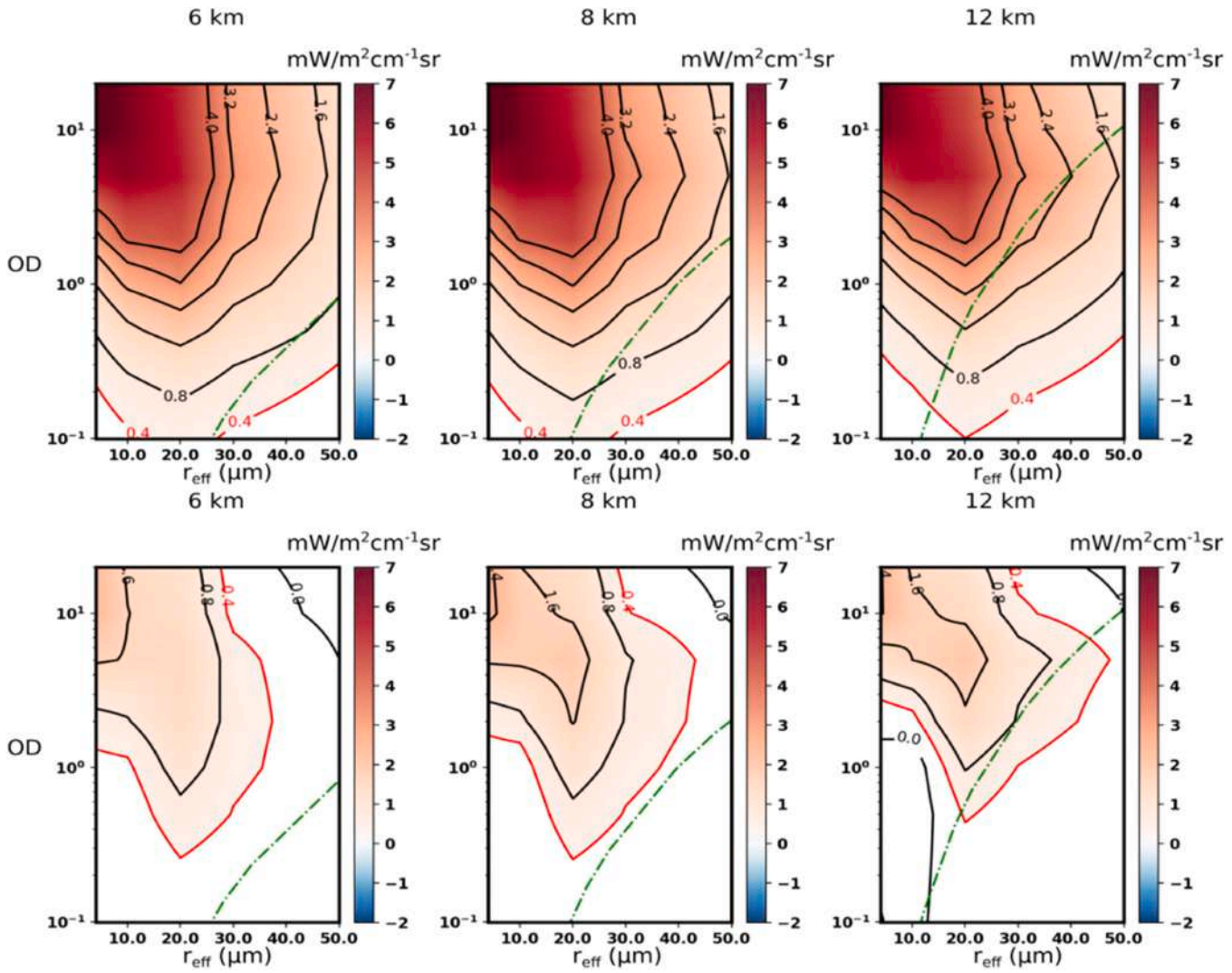

Fig. 9. Radiance differences ΔR, mW/(m2 sr cm-1), between Chou solution (upper panels) or Tang solution (lower panels) and the DISORT code as a function of multiple combinations of PSD effective radius and cloud optical depths. The 410 cm^{-1} (FIR) spectral channel is considered. The three panels of each row are for ice clouds at 6 km, 8 km, and 12 km of altitude, respectively. The white color indicates differences below the FORUM noise level, marked by the red contour line. Y-axes are in log scale. The green line indicates the OD-reff combination obtained from the Sun (2001) parametrization.

characterization of the entire radiance field which is not possible when relying on the Chou approximation only. This also enables fast and accurate computation of fluxes using Gaussian quadrature.

3. Results: evaluation of the C-mode with IASI data

The forward model σ-IASI/F2N is used to compute synthetic radiances collocated with the 16 IASI orbits described in Section 2.1. The radiance calculations are performed on the 100 to 2760 cm^{-1} spectral range. However, to simplify the comparison, we have selected six channels whose spectral location is shown in the σ-IASI/F2N spectrum of Fig. 10. The σ-IASI/F2N calculations are convolved with the IASI instrument spectral function [38]. In this way, we can adequately compare calculated and observed IASI radiances.

The rationale behind the comparison is to check the capability of σ-IASI/F2N to follow the observed pattern of spatial clouds, a combination of both the cloud modelling accuracy in our forward model and the accuracy of the ECMMF thermodynamic and cloud model fields. For clarity and conciseness, we first limit ourselves to show the comparison between Observations and Calculations (*Obs* − *Calc*) on 9 September 2021 at 0:00 UTC. The complete set of maps corresponding to the UTC hours 00:00, 06:00, 12:00, and 18:00 of 9 September 2021, encompassing IASI B and C, will be used later in this section to compile statistics for bias and standard deviation. Clearly, the comparison depends on likely discrepancies in the time-space collocation of ECMWF profiles and IASI observations. To minimize as much as possible the collocation error, we consider IASI observations that are distant ± 15 min from the ECMWF canonical hours. Even so, *Obs* − *Calc*discrepancies are expected due to many circumstances, such as the fact that the ECMWF model spatial grid of 0.05° is larger than the IASI footprint, and because of inherent limitations of the ECMWF analysis, in particular the cloud location errors [24].

Maps of computed and observed radiances in the selected channels are mapped in Figs. 11 and 12. The leftmost-hand side panel shows the channel at wavenumber 660 cm^{-1}. This channel is in the core of the CO_2 absorption band at 667 cm^{-1}; therefore, it is sensitive to the upper atmosphere, where clouds are extremely rare. And in fact, the comparison shows a smooth spatial pattern with the expected latitudinal gradients. Both the calculated and observed maps identify the tropical trough in the brightness temperature because of the higher Tropopause at that latitude. Also, calculations and observations determine the colder Stratosphere close to the Antarctic region.

Next, we consider the channel at wavenumber 791.75 cm^{-1}. The channel is in the middle of a weaker Q-branch of CO_2 and is sensitive to

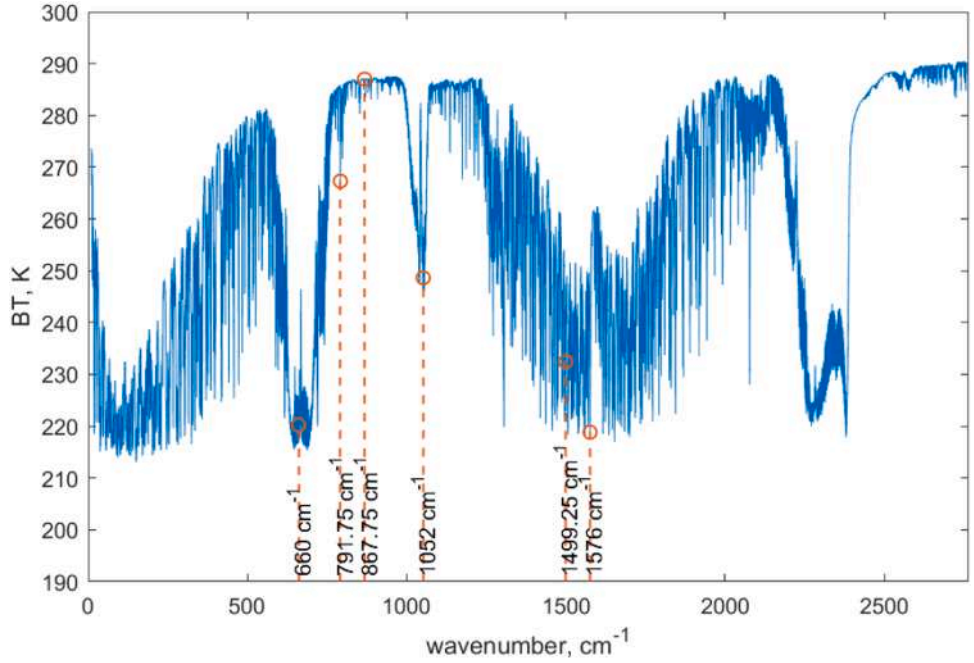

Fig. 10. Example of σ-IASI/F2N spectrum showing the spectral channels selected to check the consistency of Observations and Calculations we are dealing with in this section.

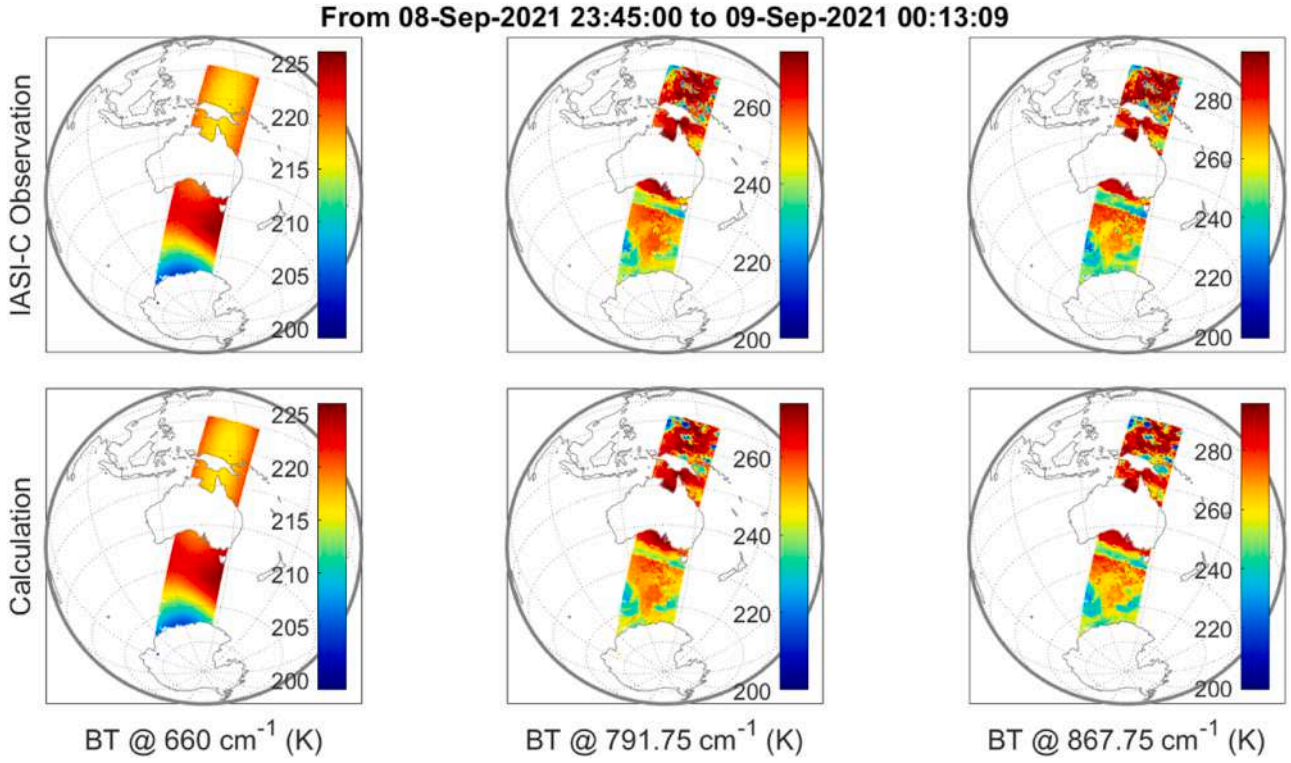

Fig. 11. Comparison of the spatial maps of the observed (IASI) and calculated (σ-IASI/F2N) radiances in the first three of six selected channels (660 cm^{-1}, 791.75 cm^{-1}, and 867.75 cm^{-1}).

the middle Troposphere. The patterns in the related maps show the structure of the middle tropospheric cloudiness. Again, we notice consistency between calculations and observations regarding the spatial structure.

The channel at wavenumber 867.75 cm^{-1} in the atmospheric window is sensitive to the surface and lower clouds. Therefore, in this channel we expect a somewhat more significant variability; in fact, we see that the range of brightness temperatures goes from 220 to about 300 K. Calculations reproduce well the spatial gradients observed by IASI.

The 1052.00 cm^{-1} channel is in the middle of the ozone band at 9.7 μm. We expect less absorption in the tropics than at mid-high latitudes because of the diverse Tropopause height. In September, we also expect

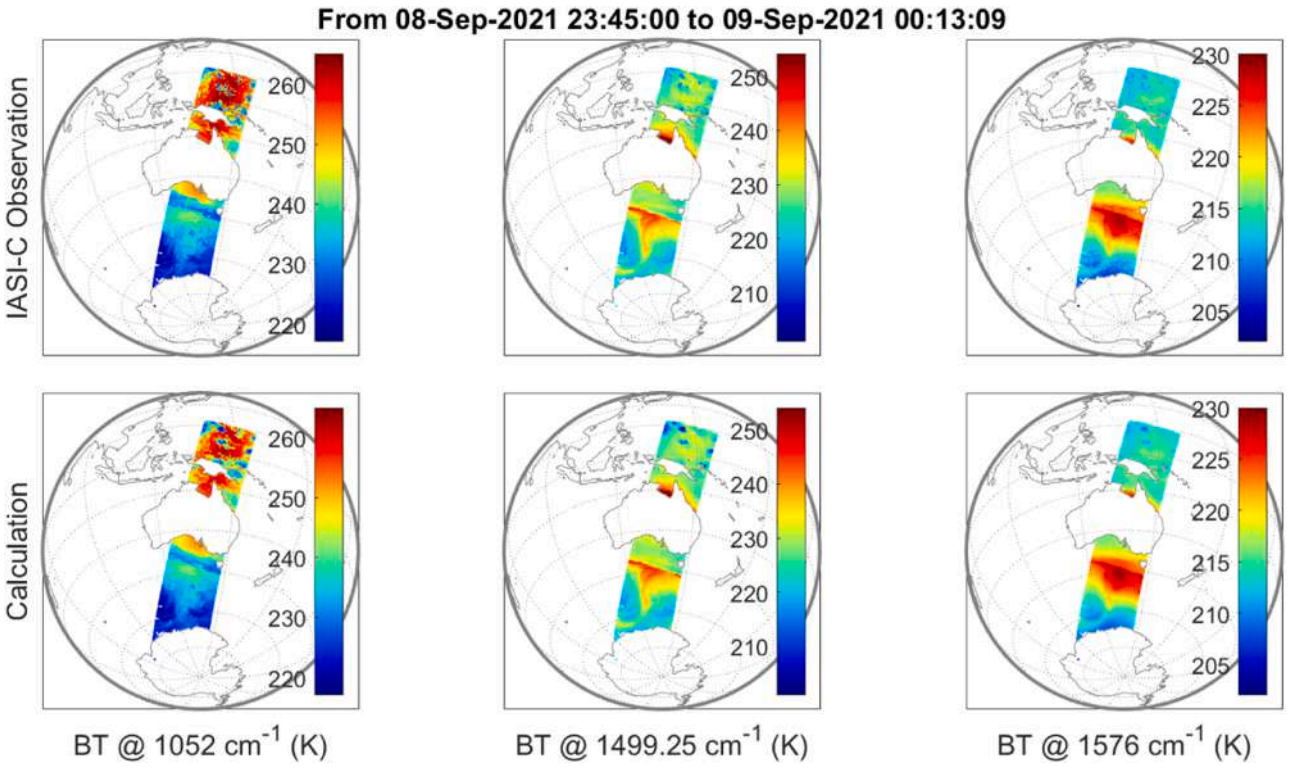

Fig. 12. As in Fig. 11 but in the last three selected channels (1052 cm^{-1}, 1499.25 cm^{-1}, and 1576 cm^{-1}).

the Tropopause to be lower in the Southern Hemisphere. Therefore, the brightness temperature in this channel is expected to be lower in the South than in the North. Observations and calculations both reproduce the expected patterns.

Next, we come to the channel at 1499.25 cm^{-1}, which is within the water vapor band at 6.7 μm and is mostly influenced by the emission of the middle Troposphere. We expect to observe the pattern of the humidity fields and their variability also because of cloud patterns. Once again, calculations reproduce accurately the spatial temperature gradients as seen by IASI.

Finally, the results at 1576 cm^{-1} are shown on the rightmost-hand side of Fig. 12. The channel is within the water vapor band at 6.7 μm, but unlike the previous one, this channel is mostly sensitive to the upper Troposphere. Therefore, we expect to observe the higher altitude patterns of the humidity field. As shown by both observations and calculations, the spatial patterns are smoother than those associated with the channel at 1499.25 cm^{-1}.

Fig. 12 shows that σ-IASI/F2N can follow the spatial patterns of cloud fields, in addition to features characteristics of *T, Q, O* fields. We underline that the ECMWF model is unanimously considered a reference Numerical Weather Prediction (NWP) system [39]. Therefore, for channels that are sensitive to *T, Q, O*, we expect a good consistency between observations and calculations.

A detailed comparison is the objective of the remainder of this section. We consider the six channels described above, but all the observations shown in Fig. 1 are accounted for (and not only one single IASI orbit). The same criterion accounting for a time difference <15 min is assumed. Moreover, a criterion concerning the state of the scene is added: if the AVHRR IASI native cloud masque and the ECMWF total cloud content are equal to 100 % (cloudy sky) or 0 % (clear sky), the data is retained and analysed. By applying this rule 32,364 IASI cloudy soundings and 2269 clear sky soundings are left for comparison. However, even with this reduced time slot of ½ hour, we expect the cloudy sky to have some remaining collocation problems. In contrast, we expect fewer problems for a clear sky because the variation of *T, Q, O* fields has characteristic time scales longer than cloud properties.

The first result concerns the cloudy sky case and is reported in Fig. 13. The figure shows the histogram of the difference $\Delta = Obs - Calc$, together with the mean and standard deviation of the differences and the Pearson correlation coefficient, r^2, or simply linear correlation between *Obs* and *Calc*. Overall, we observe a good agreement between the calculated radiances with those calculated.

The histograms of the residuals for channels 660, 1499.25, and 1576 cm^{-1} which refer to the higher atmosphere, are nearly Gaussian, which suggests that the IASI measurement error mostly dominates the difference. In fact, if we look at the mean of the differences, we see that it is close to zero at 660 cm^{-1} and $\leq$ 0.5 K for the other two channels. The linear correlation is above 0.96, and the standard deviation is in the range ~0.5–1.5 K.

The histograms show more variability for the highest transmissive channels, 791.75, 867.75, and 1052 cm^{-1}. This is expected because of meteorological processes close to the surface, whose characteristic time and space scales are much shorter, and they cannot be exactly reproduced with the intrinsic limitation of the collocation system. Although for such channels, the mean difference is largely below 1.5 K, the standard deviation reaches values as large as 7.5 K and r^2 drops down to 0.85. This result exemplifies problems with a correct time-space collocation.

As for the histograms of $\Delta = Obs - Calc$ (Fig. 14) in clear sky, we see that the mean differences are below 0.3 K, standard deviations are in the range 0.3–0.7 K, and r^2 is above 0.98. In Fig. 13, the x-axis scale is the same as that used for Fig. 14, which allows us to compare the variability in cloudy and clear skies properly. The better agreement for the clear sky is partly due to a smaller variability of clear sky atmospheric parameters with respect to q_w, q_i. Therefore, the error of interpolating/extrapolating from the ECMWF grid mesh to that of the IASI soundings is attenuated.

To assess the accuracy over the entire spectral range, we produce plots (Figs. 15 to 18) comparing the average spectrum obtained from calculations to the average spectrum of the observations, which account for the whole data set. The figures show cloudy/clear and day/night

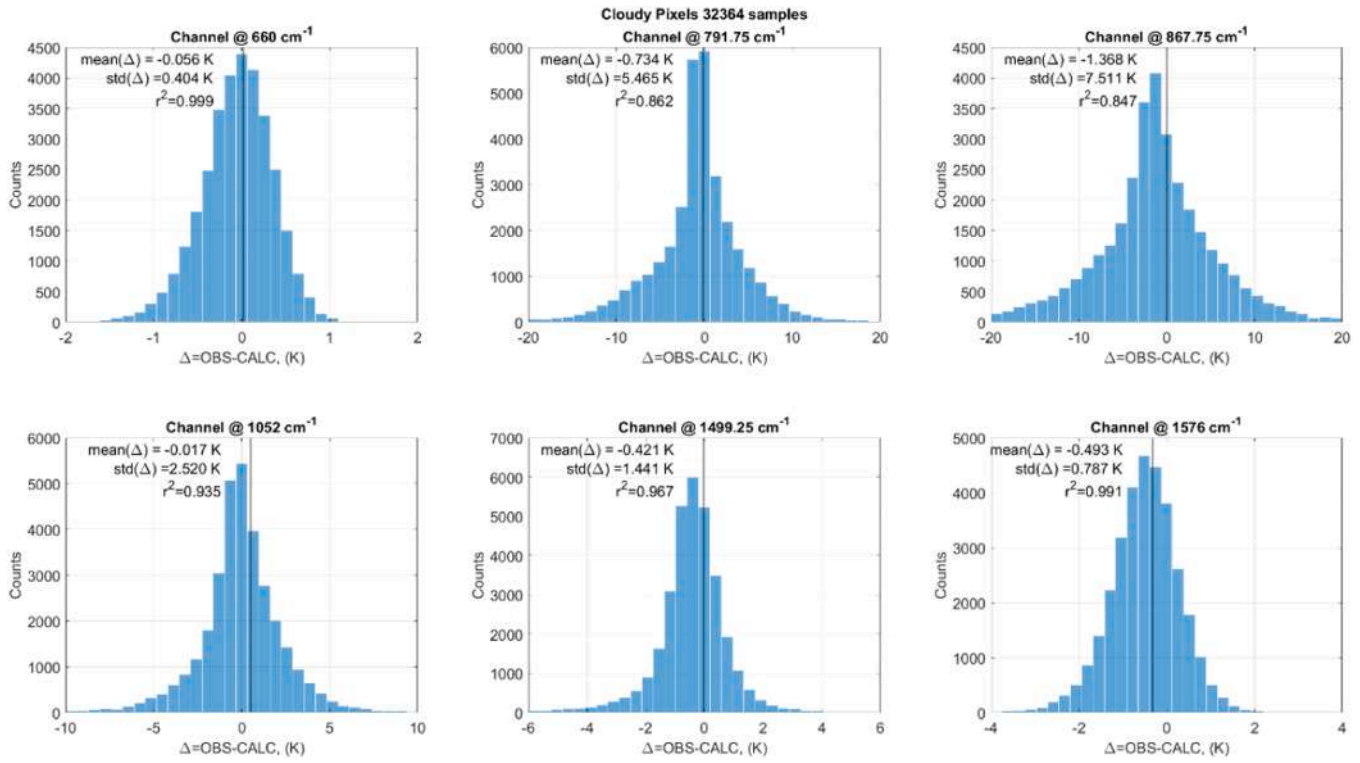

Fig. 13. Histograms of Obs-Calc for the six channels listed in Fig. 10. The difference in the figure corresponds to cloudy soundings (in the number 32,364) in the maps of Fig. 1.

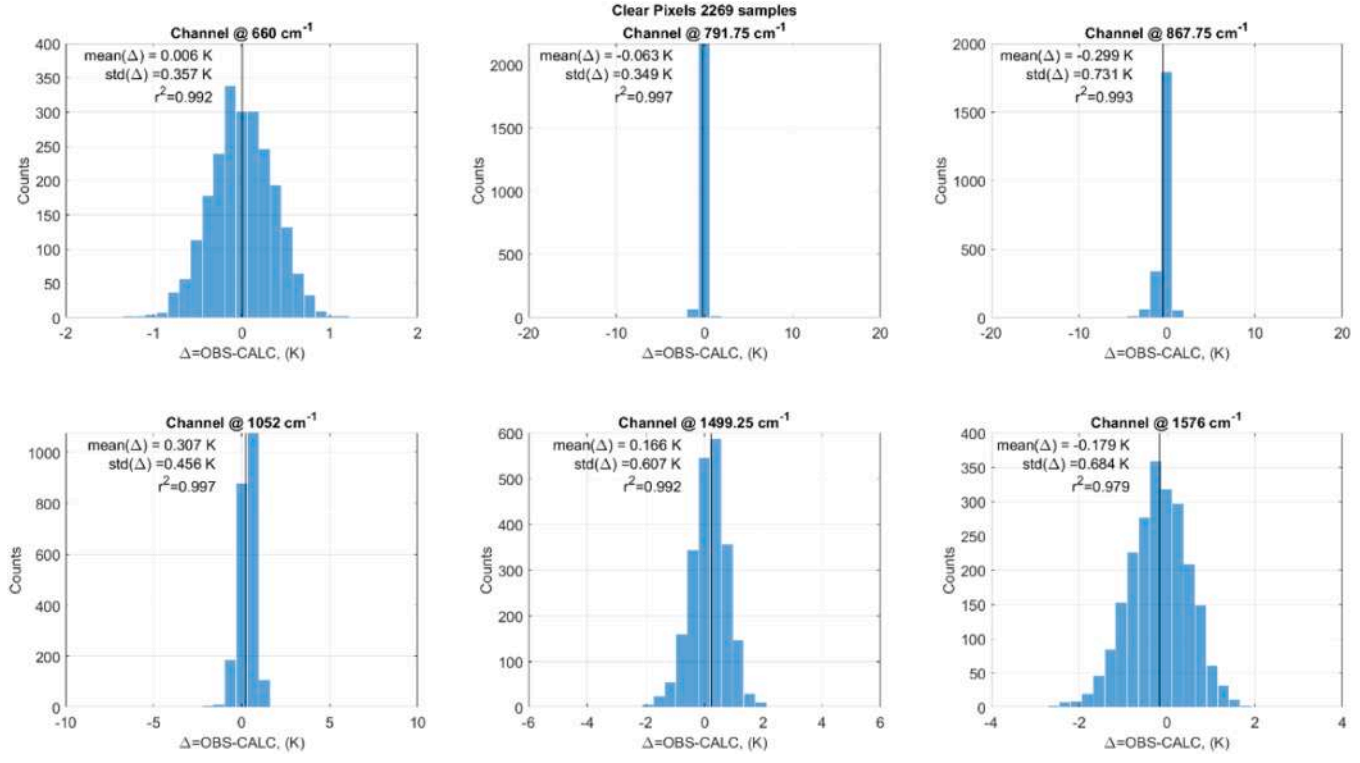

Fig. 14. Histograms of Obs-Calc for the six channels listed in Fig. 10. The difference in the figure corresponds to clear soundings (in the number 2269) in the maps of Fig. 1.

conditions separately. Clear (Fig. 15) and cloudy (Fig. 16) calculations at night agree with IASI observations within 1 K in almost all channels. The mean difference oscillates around the zero line without any systematic discrepancy, except for those expected, corresponding to gas absorption, such as CH_4, N_2O, and CO for which climatological values are assumed in the simulations.

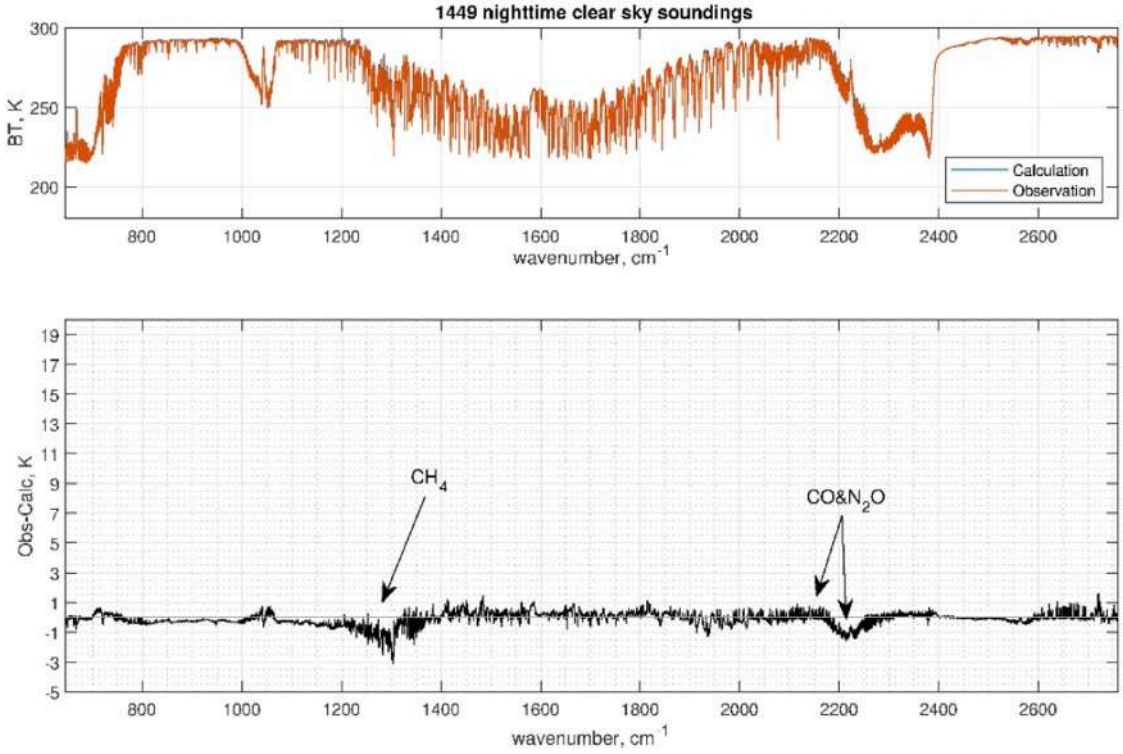

Fig. 15. Observations and Calculations averaged over the whole set of night-time clear sky soundings.

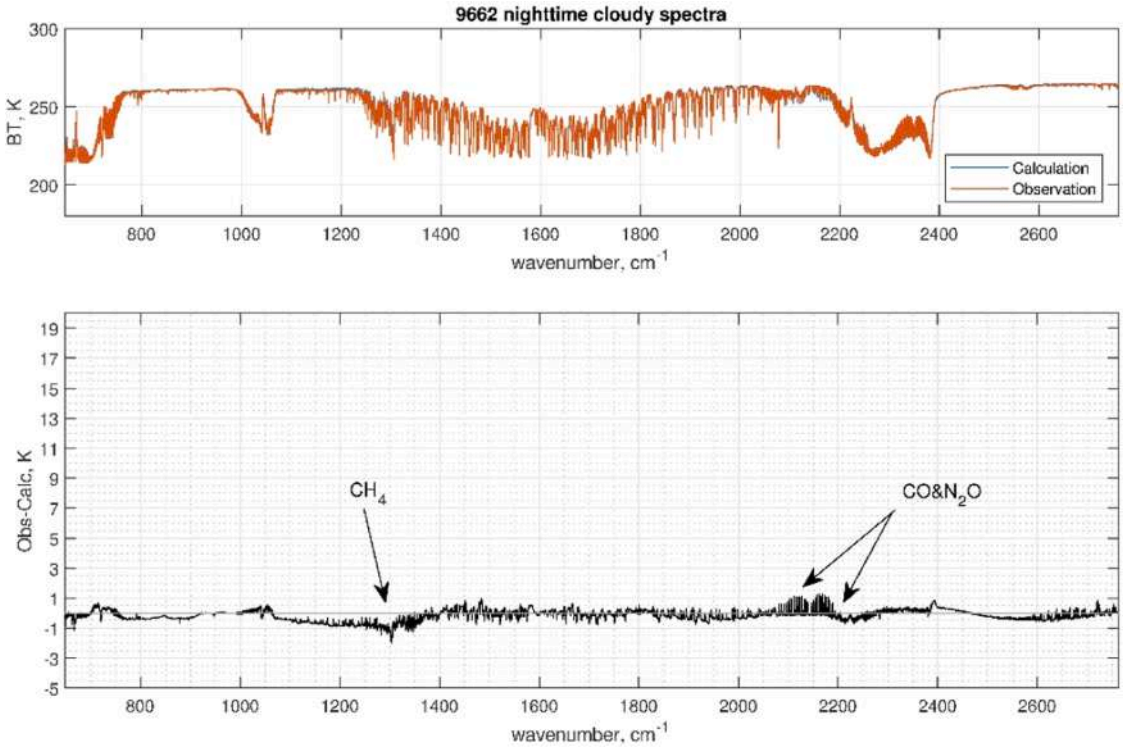

Fig. 16. Observations and Calculations averaged over the whole set of night-time cloudy sky soundings.

Conversely, for daytime, a discrepancy in the 4.3 μm absorption band of CO_2 is expected due to nonLTE (non Local Thermodynamic Equilibrium) effects, which are not accounted for in the code. The effect of nonLTE is seen in Fig. 17, which refers to daytime and clear sky. Furthermore, note the excellent agreement at the shortwave window region of the spectrum (mostly above 2400 cm^{-1}), where the reflection of solar radiation in the shortwaves needs to be considered. For this band σ-IASI/F2N assumes the Cox-Munk BRDF [34], which is appropriate for clear sky conditions over the sea.

Fig. 18 shows the comparison for the cloudy condition in the

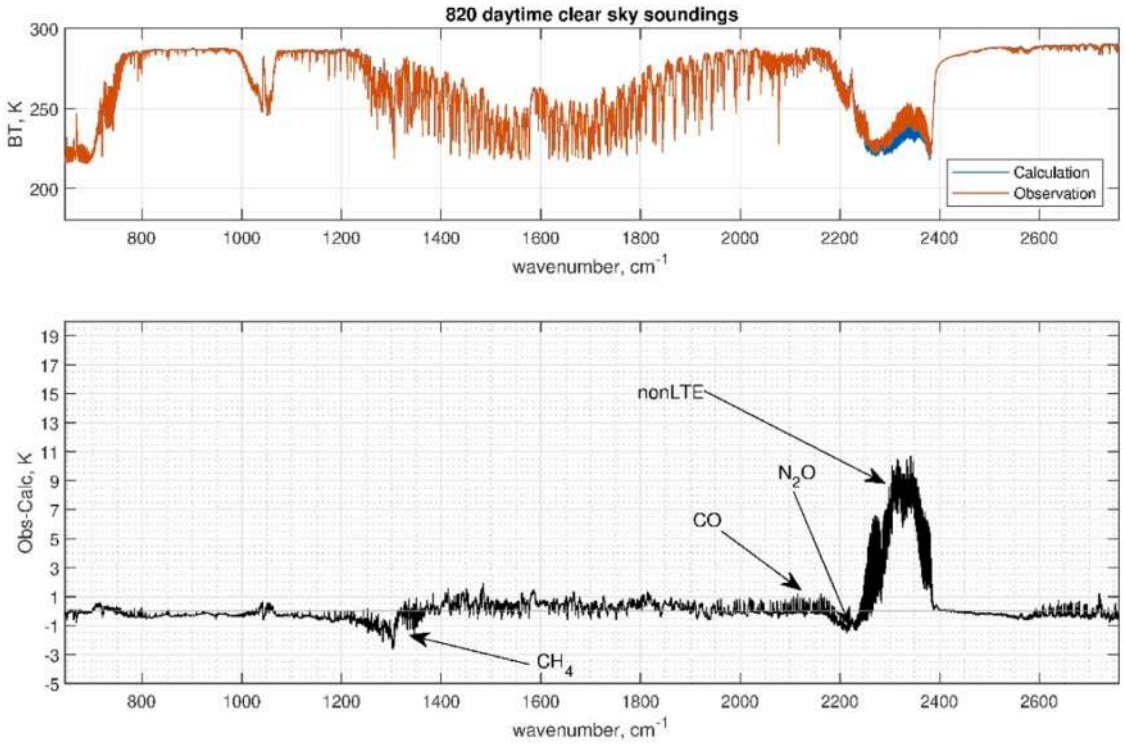

Fig. 17. Observations and Calculations averaged over the whole set of daytime clear sky soundings.

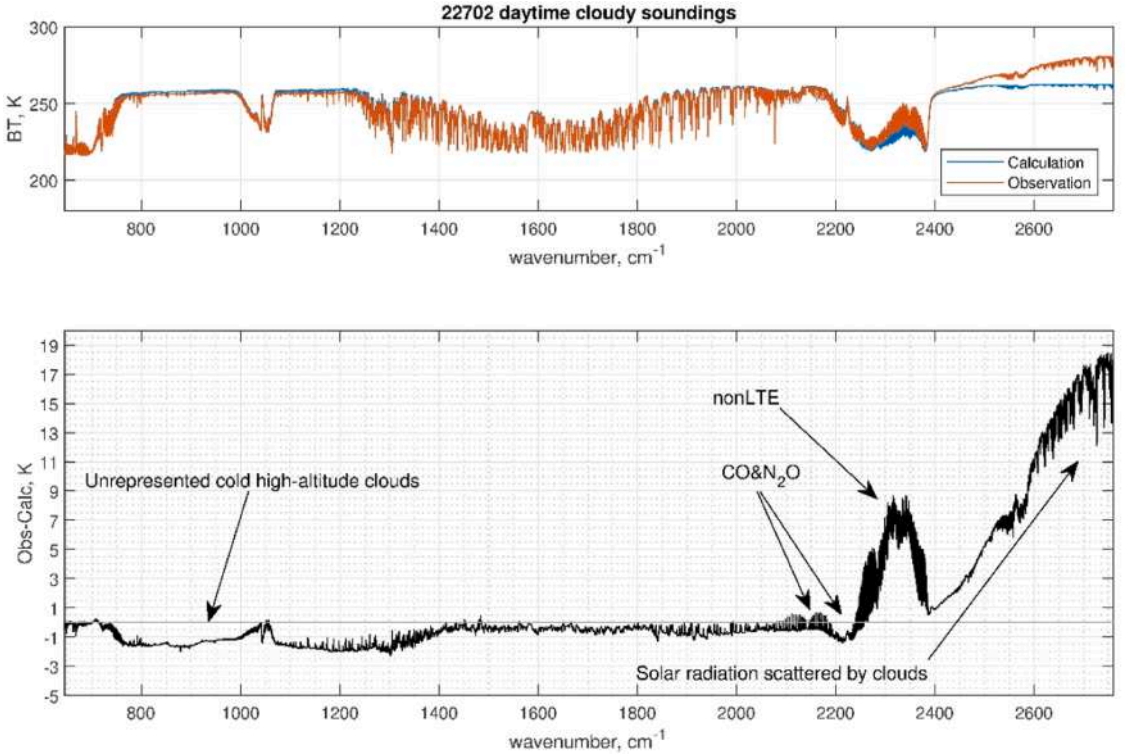

Fig. 18. Observations and Calculations averaged over the whole set of daytime cloudy sky soundings.

daytime. As expected, significant differences are obtained at around 2100 cm^{-1} because of nonLTE and above 2200 cm^{-1} spectral region because of intense scattering from clouds of solar radiation. These two processes are not yet modelled in the current version of σ-IASI/F2N. In the next version of the code we plan to adopt for the nonLTE approach adopted in SARTA fast models [33].

A systematic difference of about 1–2 K in the 8–12 μm atmospheric window is observed in the presence of clouds during the day. Note that an excellent agreement was observed for cloudy sky cases during nighttime. Since the methodology used, when compared to the full

scattering model at mid-infrared wavelengths, showed to be more accurate than 0.4 K for any cloud conditions (e.g., [2]), the result is unexpected. A possible explanation could be related to photosynthetically active Polar Stratospheric Clouds or PSC [40], which are not represented in the ECMWF analysis. PSC can yield in daylight reactive form of large nitric acid trihydrate (NAT) and ice particles, which add an aerosol load, hence absorption, in the window region. In effect, 2021 has been the year with the largest and longest Antarctic ozone hole, and its formation began in September 2021 (Krummel et al., 2022). To better analyse this issue, Fig. 19 shows the scatterplot *Calc* vs *Obs* for the soundings of 7 and for a window channel at 867.75 cm^{-1}. The scatterplot in Fig. 19 allows us to also distinguish soundings according to their latitude. We recall that we are dealing with soundings in cloudy sky during day including a large set of observations in the Antarctica and other regions in the southern Hemisphere. At tropical and mid-latitudes, the scatterplot shows both positive and negative values of the model-observation differences, which tend to compensate each other in the average. For the coldest observations at high latitudes the corresponding calculations tend to be warmer up to 10 K. This difference cannot be a bias solely in the forward model, and in fact it is not seen for most of the soundings. A possible explanation is the presence of high-altitude clouds at latitudes lower than −60° (Antarctica region), which are not represented in the ECMWF models.

4. Conclusions

We have described the extension to the FIR of the σ-IASI code, a monochromatic code intended for the fast calculations of spectral radiances and for application to the modern high spectral satellite, airborne, and ground-based spectrometers in the infrared, such as IASI, IASI-NG, FORUM. Together with the FIR extension, we have also implemented and described a LUT methodology for calculating cloud optical depths. The methodology is based on an updated description of the Chou scaling approximation [3], following the results from Martinazzo et al. [2] and a suitable polynomial parameterization, which allows us to perform a fast and accurate analytical calculation of Jacobians for cloud parameters (q_w,q_i,r_e,D_e).

At present, the code can be run in two modes. The C-mode is limited to the range of 645 to 2760 cm^{-1}. It implements the Chou scaling approximation as updated according to [2]. The C-T mode covers the whole spectral range 100 to 2760 cm^{-1} and implements the Tang-corrected Chou algorithm described in Section 2.2.3 in the far infrared, while the remaining range coincides with the C-mode. This choice is also a compromise between the computational efficiency and complexity of the code. A comprehensive comparison of Chou vs. LBLDIS has already been performed by [2]. In that work the authors adopted an updated Chou approximation. In fact, [2] computed the correct values of the *b* parameter for a large set of particle size distributions of liquid and ice clouds (assumed columns aggregates) respectively. The radiative transfer computations can thus exploit the exact backscatter parameter. This significantly improves the radiance computations upon the original parameterization proposed by Chou which is fitted for both liquid water and ice clouds without distinction.

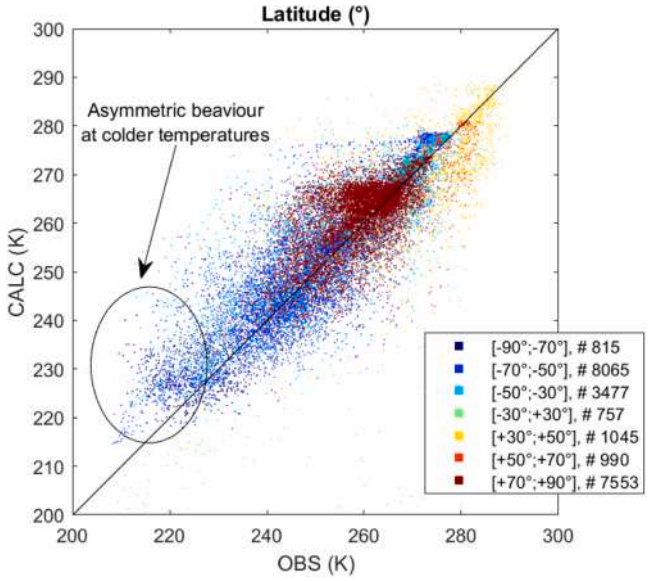

Fig. 19. Scatter plot ***Calc***vs. ***Obs*** for the window channel at 867.75 cm^{-1} of the cloudy daytime soundings. Colors refer to the latitude of the observation.

[2] show that Chou, once properly updated, performs well over the mid-infrared range. Therefore there is no need for further adjustment of Chou in this range. For the far infrared, the Tang adjustment becomes important. As shown in Section 2.2.3, the Tang correction is not a straightforward application of the *similarity principle*. We follow the Tang approach to determine a correction to the radiances, which is computationally more costly than the Chou method alone. For this reason, it is safer to apply the C-T mode where it is needed.

The C-mode code performance has been extensively validated in the spectral range 645 to 2760 cm^{-1} using a large dataset of actual IASI observations. The IASI soundings have been collocated with ECMWF analyses, which have provided the basic state vector to perform σ-IASI/F2N calculations. The model shows good agreement with IASI observations, with spectral residuals normally below ∼1 K, over the whole range of IASI spectra. In the daytime, larger discrepancies are observed, as expected, in the 4.3 μm band of CO_2 because of nonLTE (for both the cloudy and clear sky) and in the shortwave (only for cloudy sky) because of scattering effects from cloud tops. These two processes are not yet included in the code. The spectral range below 1600 cm^{-1} shows good performances for cloudy/clear and day/night conditions, which is suitable for developing a custom version for FORUM and PREFIRE.

In the perspective of applications to FORUM and PREFIRE, which also make observations below 645 cm^{-1}, we have developed a new scaling scheme in the FIR by exploiting a correction term based on the Tang methodology. The proposed approach allows simple correction coefficients that depend on the observational angles. Again, all the radiative properties (including the Tang correction coefficients) are parametrized in terms of the effective radius of the particle size distribution, thus allowing an explicit description of the cloud microphysics and the radiance analytical Jacobians computations.

The present code version can run on UNIX-based (both Linux and macOS) and Windows operating systems, and, with an Intel Xeon processor @2.70 GHz, it takes ∼1.5 s to produce the full spectrum from 10 to 2760 cm^{-1} in the complete overcast condition. With all Jacobians (gases and clouds), the time rises to 3.6 s. The new code σ-IASI/F2N is the first fast-forward module covering the spectral range from 10 to 2760 cm^{-1} with highly accurate results in the presence of multiple scattering conditions and dealing with an explicit treatment of the cloud/aerosols microphysics.

CRediT authorship contribution statement

Guido Masiello: Conceptualization, Writing- Reviewing and Editing Carmine Serio, Conceptualization, Writing- Reviewing and Editing Tiziano Maestri, Conceptualization of clouds scaling schemes, Michele Martinazzo, Implementation of Clouds scaling schemes, Fabrizio Masin, Software of Clouds properties, Giuliano Liuzzi, Data curation Writing-Reviewing and Editing Sara Venafra, Software development and Data Curation.

Declaration of Competing Interest

The authors declare that they have no known competing financial interests or personal relationships that could have appeared to influence

the work reported in this paper.

Data availability

Data will be made available on request. The current version of the code is available at https://zenodo.org/records/8152674.

Acknowledgments

The work has been partially founded by Italian Space Agency in the framework of the FIT-FORUM project. IASI was developed and built under the responsibility of CNES. It is flown onboard the Metop satellites as part of the EUMETSAT Polar System.

Appendix

In terms of numerical approximation and calculation, the most critical term in the radiative transfer equation expressed by formula (1) is atmospheric radiation,

$$R_a(\sigma) = \int_0^{+\infty} B(\sigma, T)\frac{\partial \tau}{\partial z}dz \tag{A1}$$

Considering the atmospheric layering shown in Fig. 4 and adopting the approximation of parallel-plane atmosphere, the atmospheric term can be approximated according to

$$R_a(\sigma) \approx \sum_{j=1}^{L}\left(\int_{z_{j-1}}^{z_j} B(T)\frac{\partial \tau}{\partial z}dz\right) \tag{A2}$$

so that the problem is moved to the numerical approximation of the integral

$$\int_{z_{j-1}}^{z_j} B(T)\frac{\partial \tau}{\partial z}dz \tag{A3}$$

which can be further analytically handled through the fundamental theorem of mean, which in its general formulation (e.g., [41]) establishes that

$$\int_a^b f(x)g(x)dx = f(x^*)\int_a^b g(x)dx \tag{A4}$$

with $a \le x^* \le b$ e provided that $g(x)$ does not change its sign within the interval $[a, b]$. Applying this rule to the integral (12), we have

$$\int_{z_{j-1}}^{z_j} B(T)\frac{\partial \tau}{\partial z}dz = B(T(z^*))\int_{z_{j-1}}^{z_j}\frac{\partial \tau}{\partial z}dz, \quad \text{with } z_{j-1} \le z^* \le z_j \tag{A5}$$

which considering that

$$\int_{z_{j-1}}^{z_j}\frac{\partial \tau}{\partial z}dz = \tau_j - \tau_{j-1} \tag{A6}$$

yields,

$$\int_{z_{j-1}}^{z_j} B(T)\frac{\partial \tau}{\partial z}dz = B(T(z^*))\left(\tau_j - \tau_{j-1}\right), \quad \text{with } z_{j-1} \le z^* \le z_j \tag{A7}$$

Equation (A7) is the exact solution of the integral (A3), and there is no approximation. However, Eq. (A7) holds provided that $\frac{\partial \tau}{\partial z}$ does not change the sign in the interval $[z_{j-1}, z_j]$. In effect, we have that $\tau(z)$ is of the form,

$$\tau(z) = \exp\left(-\int_z^{+\infty} k_\sigma \rho dz\right); \tag{A8}$$

hence,

$$\frac{\partial\tau}{\partial z}=\frac{\partial}{\partial z}\left(-\int_{z}^{+\infty}k_\sigma\rho dz)\right)\exp\left(-\int_{z}^{+\infty}k_\sigma\rho dz\right)=$$

$$=k_\sigma(z)\rho(z)\exp\left(-\int_{z}^{+\infty}k_\sigma\rho dz\right)\geq 0\ \forall\ z \tag{A9}$$

Therefore, Eq. (A7) is analytically correct and does not involve any approximation. Equation (A7) is the basic equation we use in σ-IASI-F2N to solve for the atmospheric radiation numerically, $R_a(\sigma)$. We stress that other schemes, such as LBLRTM, use a more crude approximation, usually called linear in τ approximation (e.g., see *Rodgers 2000*). In this approximation, integral (A3) is calculated by considering that the Planck function $B(T)$ is linear with the optical depth.

The advantage of our formulation is seen when we consider that Eq. (A7) solve the integral (A3) analytically. In a practical case, when we use the forward model for retrievals, $T(z^*)$ is guessed equal to the layer's average Temperature, $\overline{T}_j$ and its final value is that which best fits the spectral radiances.

However, in case we are not dealing with an inverse problem, the term $T(z^*)$ remains unknown, and the position $T(z^*)=\overline{T}_j$ can be a too-crude approximation, especially for cloudy skies, which in the limit of overcast conditions, make the given layer j opaque to the radiation coming from below, and the emitting Temperature becomes that of the layer top. In this case, a better guess of $T(z^*)$ is obtained by resorting to its meaning of the weighted average of the Planck function. In other words, we look for an appropriate value of $B(T(z^*))$ rather than the correct Temperature $T(z^*)$at which compute the Planck function. The approximation we are seeking relies on the fact that

$$B(T(z^*))=\frac{\int_{z_{j-1}}^{z_j}B(T)\frac{\partial\tau}{\partial z}dz}{\int_{z_{j-1}}^{z_j}\frac{\partial\tau}{\partial z}dz}=\frac{\int_{z_{j-1}}^{z_j}B(T)\frac{\partial\tau}{\partial z}dz}{(\tau_j-\tau_{j-1})} \tag{A10}$$

and we can approximate the $B(T(z^*))$ by considering the average taken on the endpoints of the interval $[z_{j-1}, z_j]$. We have

$$B(T(z^*))\approx\frac{\tau_jB(T_j)+\tau_{j-1}B(T_{j-1})}{\tau_j+\tau_{j-1}} \tag{A11}$$

which is the Planck function at the endpoints of the interval $[z_{j-1}, z_j]$ weighted with the transmittance at the same endpoints. By considering the definition of transmittance, Eq. (A11) can be cast in a more straightforward and immediate form,

$$B(T(z^*))=\frac{B(T_j)+\exp(-\nu_j)B(T_{j-1})}{1+\exp(-\nu_j)} \tag{A12}$$

where ν_j is the optical depth of the layer, j-th. The above expression also has another interesting interpretation. By exploiting the property that the Planck function is linear with Temperature (the smaller the wavenumber, the better) over temperature ranges of ∼ 10 K, we also have,

$$B(T(z^*))=\frac{B(T_j)+\exp(-\nu_j)B(T_{j-1})}{1+\exp(-\nu_j)}=B\left(T_j^*\right),$$
$$\text{with}\ \ T_j^*=\frac{T_j+\exp(-\nu_j)T_{j-1}}{1+\exp(-\nu_j)} \tag{A13}$$

Which says that $T(z^*)$ can be computed according to the effective radiative Temperature, $T_j^*(\sigma)$ (note that T_j^* depends on the wavenumber). It is seen that in the limit of $\nu_j\to 0$ (clear layer) $T_j^*\to\frac{T_j+T_{j-1}}{2}=\overline{T}_j$, which is the default value we use within σ-FORUM; conversely, in the limit $\nu_j\to+\infty$ (opaque clouds or layer), $T_j^*\to T_j$ and the radiation comes from the top of the clouds has expected. Eq. (A12) is used in the present work.

References

[1] Amato U, Masiello G, Serio C, Viggiano M. The σ-IASI code for the calculation of infrared atmospheric radiance and its derivatives. Environ Model Softw 2002;17:651–67. https://doi.org/10.1016/S1364-8152(02)00027-0.

[2] Martinazzo M, Magurno D, Cossich W, Serio C, Masiello G, Maestri T. Assessment of the accuracy of scaling methods for radiance simulations at far and mid infrared wavelengths. J Quant Spectrosc Radiat Transf 2021;271:107739. https://doi.org/10.1016/j.jqsrt.2021.107739.

[3] Chou MD, Lee KT, Tsay SC, Fu Q. Parameterization for cloud longwave scattering for use in atmospheric models. J Clim 1999;12:159–69. https://doi.org/10.1175/1520-0442(1999)012<0159:PFCLSF>2.0.CO;2.

[4] Harries J, Carli B, Rizzi R, Serio C, Mlynczak M, Palchetti L, Maestri T, Brindley H, Masiello G. The far-infrared Earth. Rev Geophys 2008;46. https://doi.org/10.1029/2007RG000233.

[5] Palchetti L, Brindley H, Bantges R, Buehler SA, Camy-Peyret C, Carli B, Cortesi U, Bianco SD, Natale GD, Dinelli BM, Feldman D, Huang XL, C.-Labonnote L, Libois Q, Maestri T, Mlynczak MG, Murray JE, Oetjen H, Ridolfi M, Riese M, Russell J, Saunders R, Serio C. FORUM: unique far-infrared satellite observations to better understand how Earth radiates energy to space. Bull Am Meteorol Soc 2020;101:E2030–46. https://doi.org/10.1175/BAMS-D-19-0322.1.

[6] L'Ecuyer TS, Drouin BJ, Anheuser J, Grames M, Henderson DS, Huang X, Kahn BH, Kay JE, Lim BH, Mateling M, Merrelli A, Miller NB, Padmanabhan S, Peterson C, Schlegel NJ, White ML, Xie Y. The polar radiant energy in the far infrared experiment: a new perspective on polar longwave energy exchanges. Bull Am Meteorol Soc 2021;102:E1431–49. https://doi.org/10.1175/BAMS-D-20-0155.1.

[7] Aumann HH, Chahine MT, Gautier C, Goldberg MD, Kalnay E, McMillin LM, Revercomb H, Rosenkranz PW, Smith WL, Staelin DH, Strow LL, Susskind J. AIRS/AMSU/HSB on the Aqua mission: design, science objectives, data products, and processing systems. IEEE Trans Geosci Remote Sens 2003;41:253–64. https://doi.org/10.1109/TGRS.2002.808356.

[8] Hilton F, Armante R, August T, Barnet C, Bouchard A, Camy-Peyret C, Capelle V, Clarisse L, Clerbaux C, Coheur PF, Collard A, Crevoisier C, Dufour G, Edwards D, Faijan F, Fourrié N, Gambacorta A, Goldberg M, Guidard V, Hurtmans D, Illingworth S, Jacquinet-Husson N, Kerzenmacher T, Klaes D, Lavanant L, Masiello G, Matricardi M, McNally A, Newman S, Pavelin E, Payan S, Péquignot E, Peyridieu S, Phulpin T, Remedios J, Schlüssel P, Serio C, Strow L, Stubenrauch C, Taylor J, Tobin D, Wolf W, Zhou D. Hyperspectral Earth observation from IASI: five years of accomplishments. Bull Am Meteorol Soc 2012;93:347–70. https://doi.org/10.1175/BAMS-D-11-00027.1.

[9] Crevoisier C, Clerbaux C, Guidard V, Phulpin T, Armante R, Barret B, Camy-Peyret C, Chaboureau JP, Coheur PF, Crépeau L, Dufour G, Labonnote L, Lavanant L, Hadji-Lazaro J, Herbin H, Jacquinet-Husson N, Payan S, Péquignot E, Pierangelo C, Sellitto P, Stubenrauch C. Towards IASI-New Generation (IASI-NG): impact of improved spectral resolution and radiometric noise on the retrieval of thermodynamic, chemistry and climate variables. Atmos Meas Tech 2014;7:4367–85. https://doi.org/10.5194/amt-7-4367-2014.

[10] Zavyalov V, Esplin M, Scott D, Esplin B, Bingham G, Hoffman E, Lietzke C, Predina J, Frain R, Suwinski L, Han Y, Major C, Graham B, Phillips L. Noise performance of the CrIS instrument. J Geophys Res Atmos 2013;118. https://doi.org/10.1002/2013JD020457. 13,108-13,120.

[11] Serio C, Masiello G, Mastro P, Tobin DC. Characterization of the observational covariance matrix of hyper-spectral infrared satellite sensors directly from measured Earth views. Sensors 2020;20:1492. https://doi.org/10.3390/s20051492.

[12] Tang G, Yang P, Kattawar GW, Huang X, Mlawer EJ, Baum BA, King MD. Improvement of the simulation of cloud longwave scattering in broadband radiative transfer models. J Atmos Sci 2018;75:2217–33. https://doi.org/10.1175/JAS-D-18-0014.1.

[13] Marke T, Ebell K, Löhnert U, Turner DD. Statistical retrieval of thin liquid cloud microphysical properties using ground-based infrared and microwave observations. J Geophys Res Atmos 2016;121(14). https://doi.org/10.1002/2016JD025667. 558-14573.

[14] Yang P, Hioki S, Saito M, Kuo CP, Baum BA, Liou KN. A review of ice cloud optical property models for passive satellite remote sensing. Atmosphere 2018;9:499. https://doi.org/10.3390/atmos9120499.

[15] Stamnes K, Tsay SC, Wiscombe W, Jayaweera K. Numerically stable algorithm for discrete-ordinate-method radiative transfer in multiple scattering and emitting layered media. Appl Opt 1988;27:2502–9. https://doi.org/10.1364/AO.27.002502.

[16] Clough SA, Iacono MJ, Moncet JL. Line-by-line calculations of atmospheric fluxes and cooling rates: application to water vapor. J Geophys Res Atmos 1992;97:15761–85. https://doi.org/10.1029/92JD01419.

[17] Turner DD, Ackerman SA, Baum BA, Revercomb HE, Yang P. Cloud phase determination using ground-based AERI observations at SHEBA. J Appl Meteorol Climatol 2003;42:701–15. https://doi.org/10.1175/1520-0450(2003)042. <0701:CPDUGA>2.0.CO;2.

[18] Heidinger AK, Li Y, Baum BA, Holz RE, Platnick S, Yang P. Retrieval of cirrus cloud optical depth under day and night conditions from MODIS Collection 6 cloud property data. Remote Sens 2015;7:7257–71. https://doi.org/10.3390/rs70607257.

[19] Heilliette S, Garand L. A practical approach for the assimilation of cloudy infrared radiances and its evaluation using airs simulated observations. Atmosphere-Ocean; 2010. https://doi.org/10.3137/ao.450403.

[20] Liuzzi G, Masiello G, Serio C, Meloni D, Di Biagio C, Formenti P. Consistency of dimensional distributions and refractive indices of desert dust measured over Lampedusa with IASI radiances. Atmos Meas Tech 2017;10:599–615. https://doi.org/10.5194/amt-10-599-2017.

[21] Liuzzi G, Masiello G, Serio C, Venafra S, Camy-Peyret C. Physical inversion of the full IASI spectra: assessment of atmospheric parameters retrievals, consistency of spectroscopy and forward modelling. J Quant Spectrosc Radiat Transf 2016;182:128–57. https://doi.org/10.1016/j.jqsrt.2016.05.022.

[22] Saunders R, Hocking J, Turner E, Rayer P, Rundle D, Brunel P, Vidot J, Roquet P, Matricardi M, Geer A, Bormann N, Lupu C. An update on the RTTOV fast radiative transfer model (currently at version 12). Geosci Model Dev 2018;11:2717–37. https://doi.org/10.5194/gmd-11-2717-2018.

[23] Matricardi M. The inclusion of aerosols and clouds in RTIASI, the ECMWF fast radiative transfer model for the infrared atmospheric sounding interferometer. ECMWF Tech. Memo. 2005;474. https://doi.org/10.21957/1KRVB28QL.

[24] Aumann HH, Chen X, Fishbein E, Geer A, Havemann S, Huang X, Liu X, Liuzzi G, DeSouza-Machado S, Manning EM, Masiello G, Matricardi M, Moradi I, Natraj V, Serio C, Strow L, Vidot J, Wilson RC, Wu W, Yang Q, Yung YL. Evaluation of radiative transfer models with clouds. J Geophys Res Atmos 2018;123:6142–57. https://doi.org/10.1029/2017JD028063.

[25] Martin GM, Johnson DW, Spice A. The measurement and parameterization of effective radius of droplets in warm stratocumulus clouds. J Atmos Sci 1994;51:1823–42. https://doi.org/10.1175/1520-0469(1994)051. <1823:TMAPOE>2.0.CO;2.

[26] Wyser K. The effective radius in ice clouds. J Clim 1998;11:1793–802. https://doi.org/10.1175/1520-0442(1998)011. <1793:TERIIC>2.0.CO;2.

[27] Grieco G, Masiello G, Matricardi M, Serio C, Summa D, Cuomo V. Demonstration and validation of the φ-IASI inversion scheme with NAST-I data. Q J R Meteorol Soc 2007;133:217–32. https://doi.org/10.1002/qj.162.

[28] Anderson, G., Clough, S., Kneizys, F., Chetwynd, J., Shettle, E., 1986. AFGL Atmospheric Constituent Profiles (0.120km) 46.

[29] WDCGG (World Data Centre for Greenhouse Gases) [WWW Document], 2016. URL https://gaw.kishou.go.jp/publications/summary (accessed 2.23.23).

[30] Howell JR, Mengüc MP, Daun K, Siegel R. Thermal radiation heat transfer. 7th ed. Boca Raton: CRC Press; 2020. https://doi.org/10.1201/9780429327308.

[31] Elsasser WM. Heat transfer by infrared radiation in the atmosphere. Harvard University. Milton, Mass: Blue Hill meteorological observatory; 1942.

[32] Liou KN. Radiation and cloud processes in the atmosphere: theory, observation and modeling. Oxford monographs on geology and geophysics. Oxford, New York: Oxford University Press; 1992.

[33] DeSouza-Machado S, Strow LL, Motteler H, Hannon S. kCARTA: a fast pseudo line-by-line radiative transfer algorithm with analytic Jacobians, fluxes, nonlocal thermodynamic equilibrium, and scattering for the infrared. Atmos Meas Tech 2020;13:323–39. https://doi.org/10.5194/amt-13-323-2020.

[34] Jackson Christopher R, Alpers W. The role of the critical angle in brightness reversals on sunglint images of the sea surface. J Geophys Res Oceans 2010;115. https://doi.org/10.1029/2009JC006037.

[35] Grieco, G., Serio, C., Masiello, G., 2013. sigma-IASI-beta: a hyperfast radiative transfer code to retrieve surface and atmospheric geophysical parameters. 10.12760/01-2013-2-07.

[36] Masiello G, Matricardi M, Serio C. The use of IASI data to identify systematic errors in the ECMWF forecasts of temperature in the upper stratosphere. Atmos Chem Phys 2011;11:1009–21. https://doi.org/10.5194/acp-11-1009-2011.

[37] Hansen JE, Travis LD. Light scattering in planetary atmospheres. Sp Sci Rev 1974;16:527–610. https://doi.org/10.1007/BF00168069.

[38] Amato U, Canditiis DD, Serio C. Effect of apodization on the retrieval of geophysical parameters from Fourier-transform spectrometers. Appl Opt 1998;37:6537–43. https://doi.org/10.1364/AO.37.006537.

[39] Kramer D. Europeans shine in weather forecasting. Phys Today 2016;69:22–4. https://doi.org/10.1063/PT.3.3046.

[40] Tritscher I, Pitts MC, Poole LR, Alexander SP, Cairo F, Chipperfield MP, Grooß JU, Höpfner M, Lambert A, Luo B, Molleker S, Orr A, Salawitch R, Snels M, Spang R, Woiwode W, Peter T. Polar stratospheric clouds: satellite observations, processes, and role in ozone depletion. Rev Geophys 2021;59. https://doi.org/10.1029/2020RG000702. e2020RG000702.

[41] Smirnov, V., Ivanovic. I., n.d. Corso di matematica superiore vol, 2020. 1, 2, 3 (parte I e II), 4 (parte I e II) [WWW Document]. Ed. Riuniti. URL https://editoririuniti.it/products/corso-di-matematica-superiore-vol-1-2-3-parte-i-e-ii-4-parte-i-e-ii, (accessed 2.18.23).